

# The Role of Surface Drag in Mesocyclone Intensification Leading to Tornadogenesis within an Idealized Supercell Simulation

BRETT ROBERTS AND MING XUE

*Center for Analysis and Prediction of Storms, and School of Meteorology, University of Oklahoma, Norman, Oklahoma*

(Manuscript received 19 December 2016, in final form 22 June 2017)

## ABSTRACT

The idealized supercell simulations in a previous study by Roberts et al. are further analyzed to clarify the physical mechanisms leading to differences in mesocyclone intensification between an experiment with surface friction applied to the full wind (FWFRIC) and an experiment with friction applied to the environmental wind only (EnvFRIC). The low-level mesocyclone intensifies rapidly during the 3 min preceding tornadogenesis in FWFRIC, while the intensification during the same period is much weaker in EnvFRIC, which fails to produce a tornado. To quantify the mechanisms responsible for this discrepancy in mesocyclone evolution, material circuits enclosing the low-level mesocyclone are initialized and traced back in time, and circulation budgets for these circuits are analyzed. The results show that in FWFRIC, surface drag directly generates a substantial proportion of the final circulation around the mesocyclone, especially below 1 km AGL; in EnvFRIC, circulation budgets indicate the mesocyclone circulation is overwhelmingly barotropic. It is proposed that the import of near-ground, frictionally generated vorticity into the low-level mesocyclone in FWFRIC is a key factor causing the intensification and lowering of the mesocyclone toward the ground, creating a large upward vertical pressure gradient force that leads to tornadogenesis. Similar circulation analyses are also performed for circuits enclosing the tornado at its genesis stage. The frictionally generated circulation component is found to contribute more than half of the final circulation for circuits enclosing the tornado vortex below 400 m AGL, and the frictional contribution decreases monotonically with the height of the final circuit.

## 1. Introduction

Supercells are characterized by a persistent mesocyclone (Lemon and Doswell 1979), and the midlevel [3–6 km above ground level (AGL)] mesocyclone is understood to result mainly from tilting of vorticity associated with the vertical shear of environmental wind (Davies-Jones 1984). While all supercells feature mid-level rotation, some also develop mesocyclones below 2 km AGL, and this development can be important for tornadogenesis. Markowski et al. (1998) investigated the tendency for storms to produce tornadoes upon interacting with mesoscale boundaries during the VORTEX field experiment and found the intensification of the low-level mesocyclone during these interactions to be a critical factor. In a climatological study of mesocyclones detected by WSR-88Ds across the United States, Trapp et al. (2005) found that while only 15% of midlevel mesocyclones were associated with tornadoes, more than

40% of low-level (below 1 km AGL) mesocyclones were tornadic. More recently, high-resolution modeling studies have also implicated the intensification of the low-level mesocyclone in supercell tornadogenesis (Mashiko et al. 2009; Schenkman et al. 2014). The dynamical link between the low-level mesocyclone intensification and tornadogenesis may be complex and multifaceted. One potential instigating factor is the enhancement of low-level updraft via pressure drops aloft (Grasso and Cotton 1995; Wicker and Wilhelmson 1995; Noda and Niino 2010), which can augment stretching of vertical vorticity near the ground within an incipient vortex. Low-level mesocyclone intensification may also be associated with rear-flank downdraft (RFD) momentum surges (Schenkman et al. 2016), which can aid in tornadogenesis (Schenkman et al. 2014) and tornado maintenance (Marquis et al. 2012), particularly when parcels constituting the surge have a relatively modest potential temperature deficit (Lee et al. 2012; Skinner et al. 2014).

In more recent years, the potentially important role of surface drag in supercell dynamics and tornadogenesis

---

*Corresponding author:* Ming Xue, mxue@ou.edu

DOI: 10.1175/JAS-D-16-0364.1

© 2017 American Meteorological Society. For information regarding reuse of this content and general copyright information, consult the [AMS Copyright Policy \(www.ametsoc.org/PUBSReuseLicenses\)](http://www.ametsoc.org/PUBSReuseLicenses).

has received increased interest in the severe storms research community. [Schenkman et al. \(2014\)](#), hereafter [S14](#)) analyzed tornadogenesis processes within a 50-m simulation obtained earlier in [Xue et al. \(2014\)](#), which assimilated Doppler radar and other observations from the 8 May 2003 tornado case in Oklahoma. This study was one of the first realistic tornado simulations employing realistic heterogeneous environmental conditions with full model physics including surface friction; most earlier tornado modeling studies used horizontally homogeneous environmental conditions defined by a single sounding, and surface friction was not considered. Individual trajectory budgets were analyzed for parcels entering two different tornadoes produced by the simulated storm. These budgets showed drag to play a dominant role in generating horizontal vorticity, which was ultimately tilted into the vertical and stretched within the tornadoes. Specifically, drag generated large horizontal vorticity within an RFD momentum surge (environmental inflow) in the first (second) simulated tornado. The dominance of frictional<sup>1</sup> vorticity for trajectories entering the first tornado suggests the possibility that even when large baroclinic vorticity is available in close proximity to a developing vortex, there may be some cases in which frictional vorticity is nonetheless an important source.

[Mashiko \(2016a\)](#), hereafter [MS16a](#)) analyzed a mesocyclone in their 50-m simulation of the 6 May 2012 tornadic supercell that struck Tsukuba City, Japan. Notably, this simulation used a heterogeneous, realistic initial condition derived from the Japan Meteorological Agency (JMA) operational mesoscale model analysis. In analyzing a material circuit initialized enclosing the low-level mesocyclone about 2 min prior to tornadogenesis, [MS16a](#) found that the circulation about the circuit had doubled during the preceding 15 min. Most of this increase in circulation owed to baroclinic forcing, but frictional forcing had a nonnegligible secondary contribution. [Mashiko \(2016b\)](#), hereafter [MS16b](#)) performed analyses of tornadogenesis in the same simulation. In the case of a material circuit initialized at 150 m AGL encircling the tornado at genesis time, a similar result was found to that for the low-level mesocyclone: most of the increase in circulation over the preceding 15 min owed to baroclinic forcing, but frictional forcing was a secondary positive contributor. In [MS16b](#), an RFD outflow surge is said to trigger tornadogenesis, implying the presence of a mature cold pool near the tornado. [MS16b](#) performed a sensitivity experiment in which

evaporation of rain and melting of ice-phase hydrometeors were disabled, preventing diabatic cooling. A vortex also developed in this experiment, but was substantially weaker than the one in the control run. Circulation analysis of a material circuit about the tornado in the sensitivity experiment without diabatic cooling suggested that friction contributed a large proportion of the circulation around its weaker vortex, although the integrated and interpolated circulation values did not agree especially well.

[Roberts et al. \(2016\)](#), hereafter [R16](#)) conducted idealized simulations of a supercell to assess the impact of surface drag on tornadogenesis. Unlike in [MS16a](#), the simulations of [R16](#) were initialized with a single sounding and lacked terrain. Two simulation experiments were performed and compared. In one experiment, the surface drag was applied to the full wind [referred to as full-wind friction (FWFRIC)] while in the other experiment, the surface drag was applied to the environmental wind only (EnvFRIC). The environmental wind profile was set up to be in balance among the Coriolis, environmental horizontal pressure gradient, and frictional forces in the experiments. A tornado developed in FWFRIC only 1500 s into the simulation, before a mature cold pool was established, suggesting a fundamentally different genesis mode than that in [MS16b](#). Through trajectory-based vorticity budget analyses, [R16](#) found direct impacts of surface friction that led to tornadogenesis in the FWFRIC experiment but not in the EnvFRIC experiment. Specifically, surface drag was found to have two roles in promoting the development of a tornado. First, drag generated new horizontal vorticity as near-ground flow accelerated toward the low-level mesocyclone, and this frictional vorticity was ultimately tilted into the vertical within and near the incipient tornado. Second, drag enhanced low-level horizontal convergence, promoting enhanced updraft near the ground, which augmented stretching of vertical vorticity, ultimately leading to a stronger low-level mesocyclone and subsequent development of a tornado.

[Markowski \(2016\)](#), hereafter [M16](#)) used highly idealized simulations to evaluate the relative roles of barotropic, frictional (“viscous”), and baroclinic vorticity in vortex genesis for supercell-like pseudostorms. Although the methodology of [M16](#) features some overlap with that of [R16](#) from a conceptual standpoint, an important difference is that the simulations of [M16](#) were dry, using an analytically defined artificial heat sink in lieu of a precipitation-driven downdraft characteristic of a supercell. Nonetheless, the idealized setup of [M16](#) made possible an array of experiments where causality is relatively straightforward. In his simulations, when an environmental sounding with primarily crosswise

---

<sup>1</sup> Throughout the paper, we will refer to horizontal vorticity generated by surface drag as frictional vorticity.

vorticity in the lowest 250 m AGL was used, a tornado-like vortex developed early in the pseudostorm evolution (similar to the full-wind drag simulation of R16). This early vortex occurred in simulations using both free-slip and semislip (i.e., containing parameterized drag) lower boundary conditions. When a different background sounding was used wherein the environmental vorticity in the lowest 250 m AGL was instead primarily streamwise, an early vortex was not observed in either the semislip or free-slip simulation; instead, a stronger vortex eventually developed later in the simulations when cool “outflow” from the heat sink reached the low-level mesocyclone. Using material circuits initialized around the vortex and traced backward in time, M16 demonstrated that frictional vorticity contributes about half of the final circulation in the semislip simulation with crosswise initial vorticity. However, the free-slip simulation initialized with the same hodograph developed a similar but stronger vortex that owed almost entirely to barotropic vorticity. This result implies that “early storm” vortex genesis in the absence of meaningful baroclinity may be possible without surface drag in cases where large crosswise near-ground vorticity is present in the environment. Nonetheless, because surface drag exists in the real world, the semislip simulations in M16 should be more realistic than their free-slip counterparts.

Collectively, the results of recent studies addressing drag’s role in high-resolution numerical simulations support the possibility of a significant role of friction in supercell tornadogenesis, and the role tends to be larger for tornadogenesis at earlier stages of storm evolution when a mature cold pool has not been established. Observations of real supercells suggest this mode is less common than “mature storm” genesis, but Doppler radars have observed storms that produced a tornado within half an hour of the first echoes (Palmer et al. 2011). Some nonsupercell tornadoes may also develop this way (Xue et al. 2016). As asserted in R16, the relevance of simulated early-storm tornadoes to supercell tornadoes in the real world is the subject of ongoing investigation. While the early-storm tornado in R16 (and in M16’s simulations with large crosswise vorticity) provides evidence for the physical plausibility of non-baroclinic vorticity sources dominating tornadogenesis dynamics in certain situations, it is unclear how often supercell tornadoes actually occur in the absence of precipitation-cooled air nearby.

While R16 studied the direct impacts of surface friction on tornadogenesis by analyzing vorticity budgets along the air parcels that feed into the tornado, it did not quantitatively investigate why the mesocyclone was much stronger and lower before tornadogenesis in the

FWFRIC case or to what degree the frictionally generated vorticity contributes to the mesocyclone circulation. It was clear in R16 that the rapid lowering and intensification of the low-level mesocyclone below 1 km AGL in FWFRIC played a crucial role in instigating tornadogenesis (see their Figs. 5 and 6). It is therefore important to understand the causes of the disparate mesocyclone evolution between FWFRIC and EnvFRIC. Furthermore, the vorticity analyses of R16 were primarily based on a representative backward parcel trajectory that was initialized within the tornado vortex at 400 m AGL. As such, questions remained regarding the vorticity source(s) for parcels entering the tornado at different heights; the same questions also apply to the preceding low-level mesocyclone. To help answer these questions, circulation analyses similar to those employed in M16, MS16a, and MS16b are performed in this study.

As a direct extension of R16, this paper analyzes the same pair of simulations (FWFRIC and EnvFRIC) but focuses primarily on the evolution and dynamics of the low-level mesocyclone preceding tornadogenesis. Circulation-based analyses of mesocyclone and tornado dynamics are performed to compliment and extend the trajectory-based analyses of R16. The remainder of this paper is organized as follows. Section 2 briefly reviews the model configuration and experimental setup described at length in R16. Section 3 presents analyses of the simulated low-level mesocyclone evolution and circulation budgets for the mesocyclone and tornado. Section 4 includes a summary, conclusions, and suggested directions for future research.

## 2. Methodology

As mentioned earlier, this study is an extension of the analysis in R16 and utilizes data from the same simulations, FWFRIC and EnvFRIC, described therein. Details of the model configuration and experimental design are found in section 2 of R16. As a brief summary, the simulations are conducted using the Advanced Regional Prediction System (ARPS) (Xue et al. 2000; Xue et al. 2001) on a grid with 50-m spacing in the horizontal. The vertical grid is stretched, with a grid spacing of 20 m near the ground that increases to 400 m above 10 km AGL. The initial condition is horizontally homogeneous, except for an artificial thermal bubble near the center of the domain used to instigate deep moist convection.

The background sounding is based on a sounding used by Dawson et al. (2010, hereafter DA10); it was extracted from a real-data 3-km simulation of the 3 May 1999 tornado outbreak in central Oklahoma, as documented in Dawson et al. (2015, hereafter DA15). This

sounding is further modified, as described in R16, such that the wind profile is in a three-force balance among the horizontal pressure gradient force (PGF), Coriolis force, and parameterized surface drag in the model. The procedure used to attain this balance and its implications were described at length in section 2b of R16. In summary, the original sounding profile used in DA10 (herein, this sounding profile is referred to as MAY3) is used to initialize a 1D column run in ARPS with surface drag enabled and the drag coefficient  $C_d = 0.01$ , as in the full 3D experiments of R16 (whose data are further analyzed in this paper). The 1.5-order TKE-based sub-grid-scale (SGS) turbulence mixing parameterization is also used, as in the full 3D simulations (note that the original extracted sounding profile had already been subject to the 1.5-order TKE-based PBL parameterization mixing in the 3-km real-data simulation, as described in DA15). The column run is integrated for 48 h in order for the profile to reach a steady state that is in a three-force balance (among the horizontal PGF, Coriolis, and internal frictional forces). The final profile at the end of this run (MAY3B) is used to initialize the 3D simulations in R16. As discussed in R16, one drawback of this methodology is that it effectively assumes the wind profile in MAY3 is geostrophic. R16 estimated that the 0–1-km storm-relative helicity (SRH) in profile MAY3B is approximately 20% larger than it would have been had the 1D column run been initialized with a better-estimated (but unknown) geostrophic wind profile.

As described in R16, in the ARPS model, the surface drag comes into the model in the form of horizontal momentum stresses defined at the ground surface [see (1) and (2) in R16], and the parameterized stresses are proportional to the drag coefficient, the surface wind speed, and the wind component on which the stress acts. Such parameterized stresses at the lower boundary replace stress tensors that would otherwise be calculated using the SGS turbulence parameterization scheme; therefore, they serve as the lower boundary conditions for the vertical fluxes of horizontal momentum within the turbulence mixing terms of the horizontal momentum equations. The effects of surface drag are propagated upward into the flow mainly through the turbulence mixing terms, which can also be called the internal frictional force.

The sole difference between experiments FWFRIC and EnvFRIC lies in the formulation of parameterized surface drag. In FWFRIC, surface drag is proportional to the full ground-relative wind speed; that is, the drag acts on the full wind, including any perturbation wind introduced by the convective storm. In EnvFRIC, however, surface drag is only applied to the environmental base-state wind (defined by our initial balanced

sounding); it does not act on perturbation winds induced by the simulated storm. The drag in EnvFRIC is therefore a spatiotemporally constant stress that acts strictly to maintain the three-force balance implicit in the environmental sounding, while leaving the storm-induced perturbation wind unaffected. The direct effect of surface drag on the simulated storm itself is excluded in EnvFRIC; this experiment can be thought of as effectively free slip, in the sense that the lower boundary condition for the vertical flux of momentum does not change based upon the local wind. More discussions on this methodology can be found in R16. In practical terms, FWFRIC is designed to illustrate how the simulated storm evolves when drag acts as it does in nature, while EnvFRIC is designed to illustrate how the storm evolves when drag only acts to create the background wind profile.

It should be noted that given the grid spacing we use (50 m in the horizontal and 20 m in the vertical near the ground), our simulations are essentially large-eddy simulations (LESs). The 1.5-order TKE-based SGS turbulence mixing scheme within ARPS, which is primarily based on Moeng and Wyngaard (1988), is therefore appropriate for our simulations. The mixing terms act to propagate the effects of surface drag into the flow interior and appear as fictional force terms on the right-hand side of the horizontal momentum equations. It is known that SGS turbulence closure schemes in LES often have issues near a rigid wall as the turbulent eddies become increasingly smaller near the wall; a special near-wall stress model has been designed to deal with such issues (Chow et al. 2005) but is not yet in common use for convective storm simulations such as those in the present study. Mason and Thomson (1992) show that typical LES schemes often overestimate the gradient of parallel velocity components near a rigid wall; this suggests that the vertical shear of the horizontal wind very close to the ground (the lowest 50 m AGL or so) may be overestimated somewhat in our simulation, but we believe the results obtained in this study should still be qualitatively valid. We also note that Markowski and Bryan (2016, hereafter MB16) examine potential problems in LESs where the environmental inflow is laminar and subject to surface drag, starting from an initial wind profile that is constant with height. In such a scenario, owing to the absence of sufficient vertical turbulence mixing, the vertical shear near the ground can be excessively large after a few hours of model integration. In our simulations, because the initial sounding has already been subject to surface drag and is in a three-force balance, the primary issue highlighted in MB16 should not apply; a more detailed discussion is given in section 3d.

### 3. Analysis of simulations

#### a. Overview of mesocyclone evolution in FWFRIC and EnvFRIC

A more complete overview of experiments FWFRIC and EnvFRIC can be found in section 3a of R16. In this subsection, we will focus specifically on the mesocyclone evolution.

Time–height sections of horizontal domainwide maximum vertical velocity are presented for FWFRIC (Fig. 1a) and EnvFRIC (Fig. 1c) for the mesocyclone development and intensification period. Beginning around 1200 s, the  $20 \text{ m s}^{-1}$  maximum updraft contour lowers toward the ground more rapidly in FWFRIC than in EnvFRIC. After 1320 s, maximum updraft below 1 km AGL strengthens rapidly in FWFRIC while remaining nearly steady in EnvFRIC. By 1350 s, the  $16 \text{ m s}^{-1}$  maximum updraft has descended below 100 m AGL; by 1400 s, updraft exceeding  $50 \text{ m s}^{-1}$  exists below 1 km AGL (Fig. 1a).

The domainwide maximum vertical vorticity begins to attain larger values in FWFRIC (Fig. 1b) than in EnvFRIC (Fig. 1d) at around 1280 s below 1 km AGL, with the values in FWFRIC becoming much larger by 1320 s. Overall, the mesocyclone below 1 km AGL in FWFRIC intensifies markedly during the period from 1200 to 1380 s, with the most rapid intensification occurring after 1320 s. By 1500 s, vertical vorticity exceeding  $0.5 \text{ s}^{-1}$  has descended to about 100 m AGL (Fig. 1b). By comparison, the low-level mesocyclone in EnvFRIC exhibits much more modest intensification that occurs gradually from 1200 to 1500 s; by 1500 s, the maximum below 2 km AGL is only about  $0.25 \text{ s}^{-1}$  (Fig. 1d).

Vertical cross sections of perturbation pressure and vertical vorticity through the center of the low-level mesocyclone<sup>2</sup> are presented in Fig. 2 for four times at 1-min intervals during the mesocyclone intensification period. For context, horizontal cross sections of updraft, rainwater mixing ratio, and vertical vorticity are presented in Fig. 3 at the first and last of these four times, with heavy dashed lines highlighting the  $x$ – $z$  planes of the corresponding vertical sections in Fig. 2. At 1200 s, the pressure and vorticity fields are qualitatively similar between the two experiments (Figs. 2a and 2e), and this similarity continues through 1260 s (Figs. 2b and 2f), although somewhat larger cyclonic vorticity has begun to develop in FWFRIC. By 1320 s, a vertically coherent region of enhanced cyclonic vorticity is apparent in FWFRIC around  $y = 64\,000 \text{ m}$ ; pressure deficits larger

than 4 hPa extend substantially lower toward the ground in FWFRIC than EnvFRIC (Figs. 2c and 2g). Finally, at 1380 s, the negative perturbation pressure at the center of the mesocyclone has become much stronger in FWFRIC than in EnvFRIC (Figs. 2d and 2h). The zone of relatively small pressure deficits near the ground centered around  $y = 64\,500 \text{ m}$  in both experiments is the storm-scale convergence boundary, directly above which the strongest cyclonic vorticity exists in the mesocyclone. It is noteworthy that the perturbation pressure contours above the boundary are oriented more horizontally in FWFRIC (Fig. 1d) than in EnvFRIC (Fig. 1h), illustrating that the mesocyclone in FWFRIC is not only stronger overall but has more effectively lowered toward the ground over a broad extent.

Corresponding vertical cross sections of vertical perturbation pressure gradient force (VPPGF) and vertical velocity are presented in Fig. 4. From 1200 to 1260 s, these fields appear remarkably similar between the two experiments (Figs. 4a,b and 4e,f). At 1320 s, the upward-directed VPPGF around 500 m AGL has become modestly stronger in FWFRIC than in EnvFRIC (Figs. 4c and 4g). By 1380 s, this discrepancy has become much larger, with VPPGF values at 500 m AGL in FWFRIC more than double those in EnvFRIC (Figs. 4d and 4h). The  $20 \text{ m s}^{-1}$  updraft contour has also descended to 400 m AGL in FWFRIC, while it remains at around 600 m AGL in EnvFRIC. Based on these vertical sections, it is apparent that the larger VPPGF is dominantly driving the enhanced updraft below 1 km AGL in FWFRIC, particularly as thermal buoyancy is negligible in this region at this stage of the simulation in both experiments (not shown).

Based on the analysis above, the intensification of the low-level mesocyclone in FWFRIC appears to involve a positive feedback cycle. This cycle consists of two processes. First,<sup>3</sup> the stronger updraft above the sharper surface convergence boundary in FWFRIC (cf. Fig. 4 in R16) enhances vertical stretching of environmental vorticity (after it is tilted) and leads to a stronger mesocyclone. Larger vorticity within the stronger mesocyclone produces larger pressure deficits via the “spin” term of the dynamic pressure equation. Second, the reduced pressure around 1 km AGL in FWFRIC increases the VPPGF immediately below, further augmenting the updraft and intensifying the vertical vorticity through stretching. This process also effectively lowers the base of the mesocyclone and further increases the near-ground VPPGF. Thus, a positive feedback exists between the intensification of updraft and

<sup>2</sup>The center point was chosen manually at each plotted time by identifying the mesocyclone’s center of circulation at 1000 m AGL.

<sup>3</sup>We do not use “first” or “second” in a chronological sense here, as it is not entirely clear which of the two processes initiates the feedback cycle.

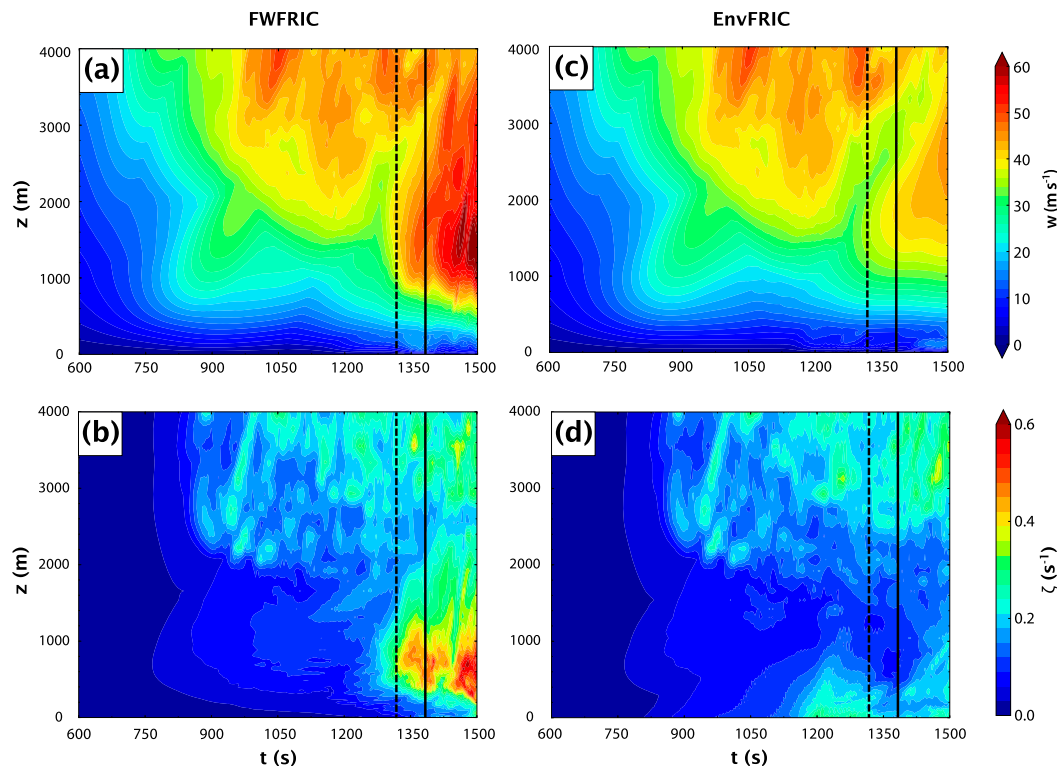


FIG. 1. Domainwide time–height cross sections between 600 and 1500 s for FWFRIC of (a) maximum updraft and (b) maximum vertical vorticity. The dashed and solid black lines denote times  $t = 1320$  and  $1380$  s, respectively. (c),(d) As in (a) and (b), respectively, but for EnvFRIC.

vertical vorticity in the low-level mesocyclone. This type of feedback is common in the midlevel mesocyclone as a supercell develops and intensifies, but in this case, the feedback appears also to occur closer to the ground where environmental vorticity is a less effective source of vertical vorticity (Davies-Jones 1984). The vorticity dynamics of the mesocyclone intensification will be analyzed in the following subsection. We will see that the tilting of horizontal vorticity generated by surface friction also plays an important role in the mesocyclone intensification.

#### b. Circulation analyses of material circuits enclosing the mesocyclone

To clarify the physical processes contributing to vertical vorticity in the low-level mesocyclone, material circuits are initialized within horizontal planes at various heights; the circuits are constructed such that they closely enclose the mesocyclone at various times. Rotunno and Klemp (1985) first employed material circuits to analyze mesocyclone dynamics within a supercell simulation. In the present study, the material circuits are formed by individual parcels whose trajectories are integrated backward in time using the fourth-order Runge–Kutta method (as in R16) using a 0.5-s integration time step (via temporal

interpolation of model output wind fields, which are available every 2 s). When a material circuit is initialized, parcels are placed along the circuit approximately 19 m apart. The initial circuits are circular and contained within a horizontal plane. During backward integration of the trajectories, at each time step, the three-dimensional distance between each pair of adjacent parcels is checked. If this distance exceeds 25 m, a new parcel is initialized at the midpoint of the line segment joining the two parcels. As such, the number of parcels comprising the circuit can increase during integration as needed. This technique of parcel addition for circuit analysis was also employed by Markowski and Richardson (2014); its purpose is to ensure that the circuit is properly sampled along its entire extent, avoiding the development of large gaps between parcels on the circuit.

The circulation about a material circuit is defined as

$$C = \oint \mathbf{v} \cdot d\mathbf{l}, \quad (1)$$

where  $\mathbf{v}$  is the velocity vector and  $d\mathbf{l}$  is a segment of circuit (directed counterclockwise). Kelvin's circulation theorem states that in the barotropic limit and with conservative body forces, circulation is a conserved

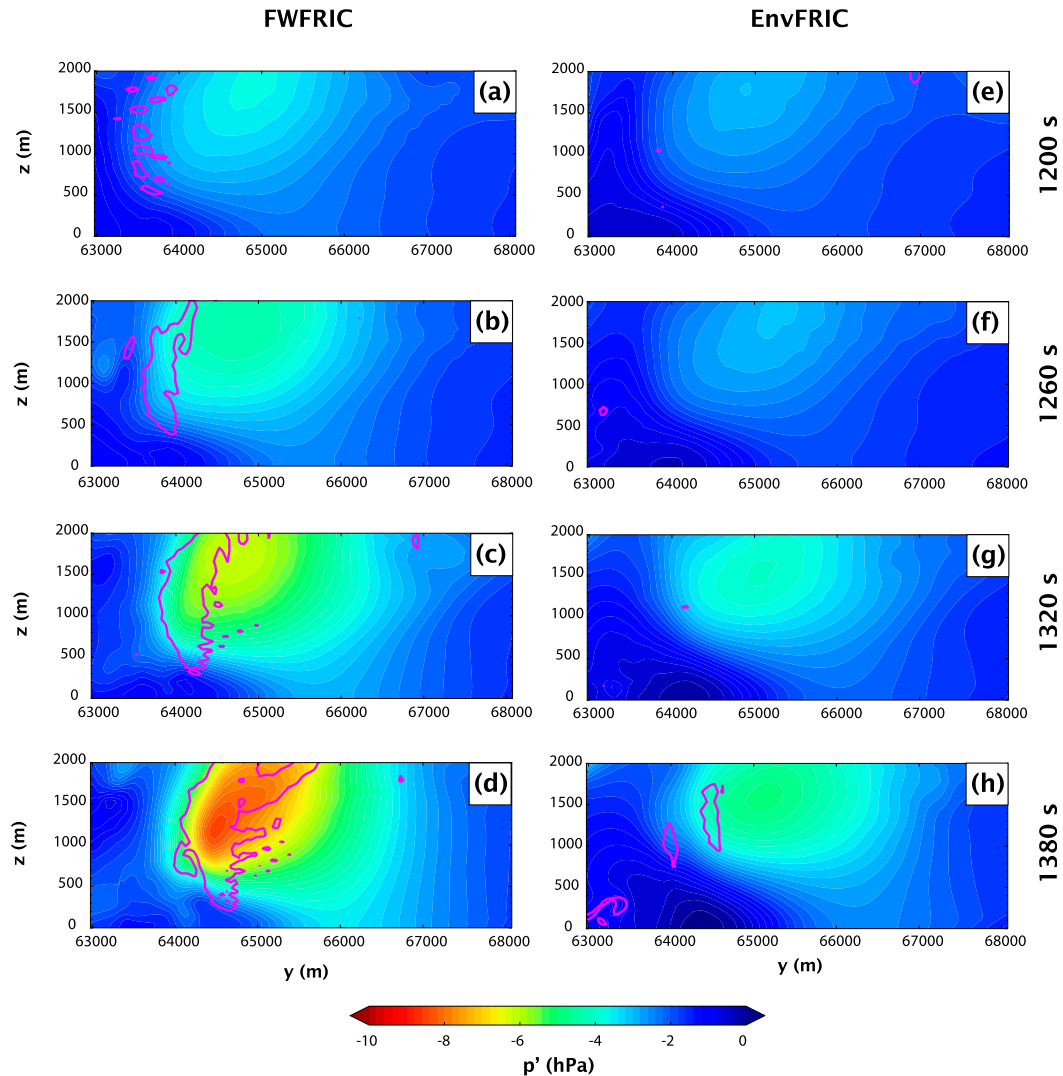


FIG. 2. (left) Vertical meridional cross section through the mesocyclone center in FWFRIC of perturbation pressure (shaded) and the  $0.05\text{-s}^{-1}$  vertical vorticity contour (magenta) at (a) 1200 s ( $x = 35\,875\text{ m}$ ), (b) 1260 s ( $x = 35\,875\text{ m}$ ), (c) 1320 s ( $x = 35\,875\text{ m}$ ), and (d) 1380 s ( $x = 35\,775\text{ m}$ ). (right) The corresponding plots for EnvFRIC are given for (e) 1200 s ( $x = 35\,775\text{ m}$ ), (f) 1260 s ( $x = 35\,625\text{ m}$ ), (g) 1320 s ( $x = 35\,625\text{ m}$ ), and (h) 1380 s ( $x = 35\,525\text{ m}$ ).

quantity for a material circuit. In other words, only baroclinity or nonconservative body forces (such as viscous effects) can modify the value of circulation as a circuit evolves over time. In our case, the prognostic equation for circulation can be written as

$$\frac{dC}{dt} = \oint \mathbf{F} \cdot d\mathbf{l} + \oint B dz, \quad (2)$$

where  $\mathbf{F}$  is the internal frictional force given by the SGS mixing terms. In our case, the mixing terms include both SGS turbulence mixing and computational diffusion terms; they arise out of physical and computational considerations and they act together to propagate the effect of surface drag into the flow interior. In (2)  $B$  is

buoyancy. From Stokes' theorem, circulation about a circuit is equal to the integral of vorticity over a surface bounded by the circuit, which implies that the average vorticity normal to the bounding surface is proportional to its circulation. In the case of a purely horizontal circuit then, the average vertical vorticity within the enclosed area is proportional to circulation. With this in mind, initializing horizontal material circuits enclosing the mesocyclone and tracing them backward in time enables us to trace the evolution of the bulk vorticity within the mesocyclone through circulation budgets. This not only provides a holistic assessment of the mesocyclone, but by utilizing many parcels also reduces the opportunity for the type of rapid error growth to

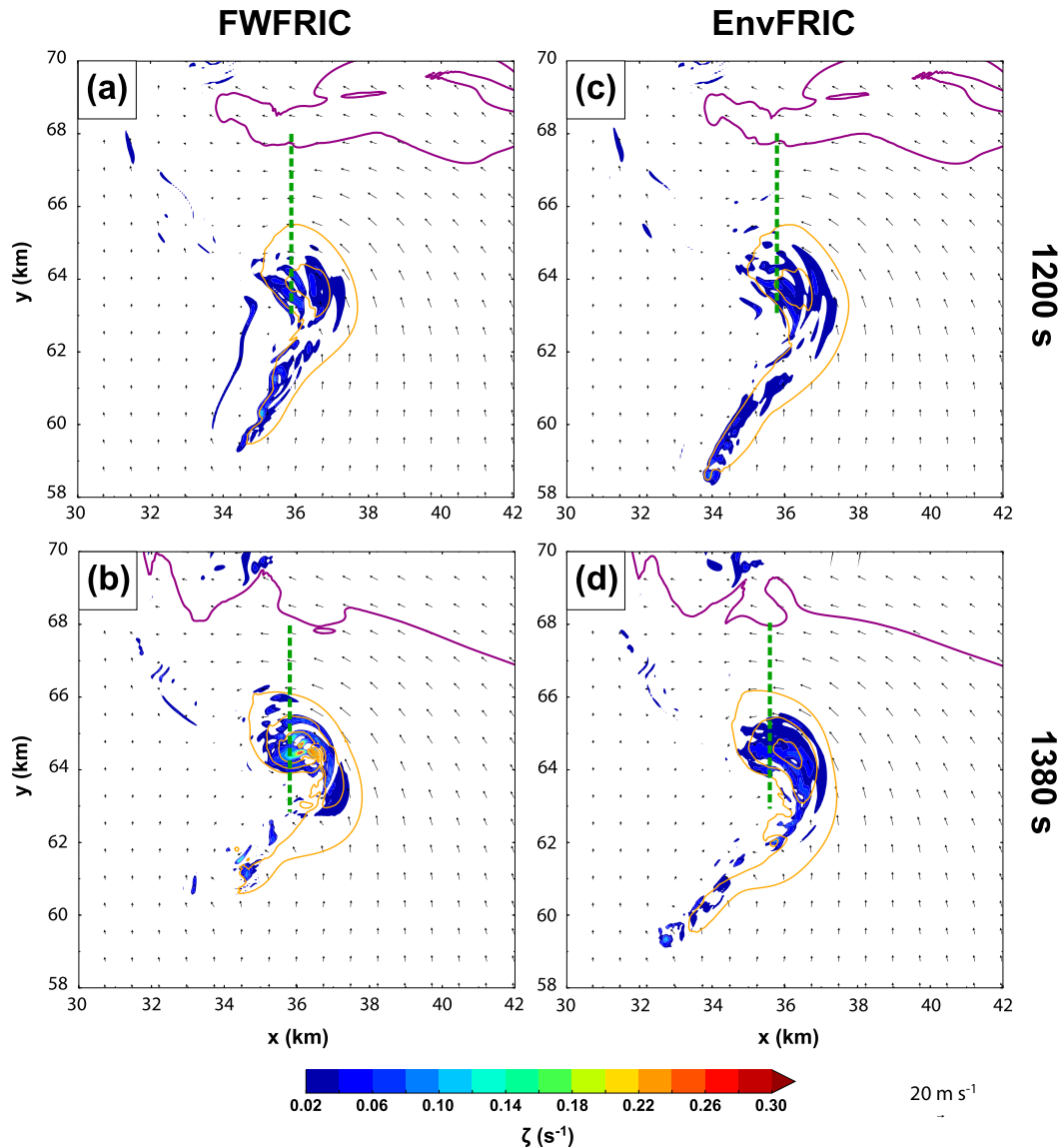


FIG. 3. Horizontal cross section at 1000 m AGL displaying the  $0.3 \text{ g kg}^{-1}$  rainwater mixing ratio contour (purple), vertical velocity contours (orange; every  $10 \text{ m s}^{-1}$  for  $w \geq 10 \text{ m s}^{-1}$ ), vertical vorticity (shaded), and wind vectors for (left) FWFRIC at (a) 1200 and (b) 1380 s and (right) EnvFRIC at (c) 1200 and (d) 1380 s. The heavy dashed green line denotes the plane of the vertical cross section for the corresponding time in Figs. 2 and 4.

which budget calculations along individual trajectories are prone.

For the analysis herein, we construct circular material circuits with a radius of 1.5 km and center them on the wind field's center of circulation (which is identified subjectively based on plotted wind vectors and is not necessarily coincident with a vorticity maximum) at the height and time of initialization. This radius allows the circuits to enclose the core of the low-level mesocyclone completely but also tends to keep constituent parcels far enough radially outward from the chaotic wind field near vorticity maxima to avoid rapid error growth in

trajectory calculations. We integrate the trajectories for parcels comprising the circuits backward for 10 min (600 s), as integrating further backward in time tends to result in extremely complex circuit shapes with unreliable circulation budgets in some cases. Here we note that when circuit parcels pass below the lowest scalar grid level in the model (10 m AGL), all quantities (besides vertical velocity  $w$  and its mixing term, which are defined at the ground level) used in the circulation budget calculations are held constant vertically within the 0–10 m AGL layer. Complications related to the treatment of near-ground parcels were discussed at

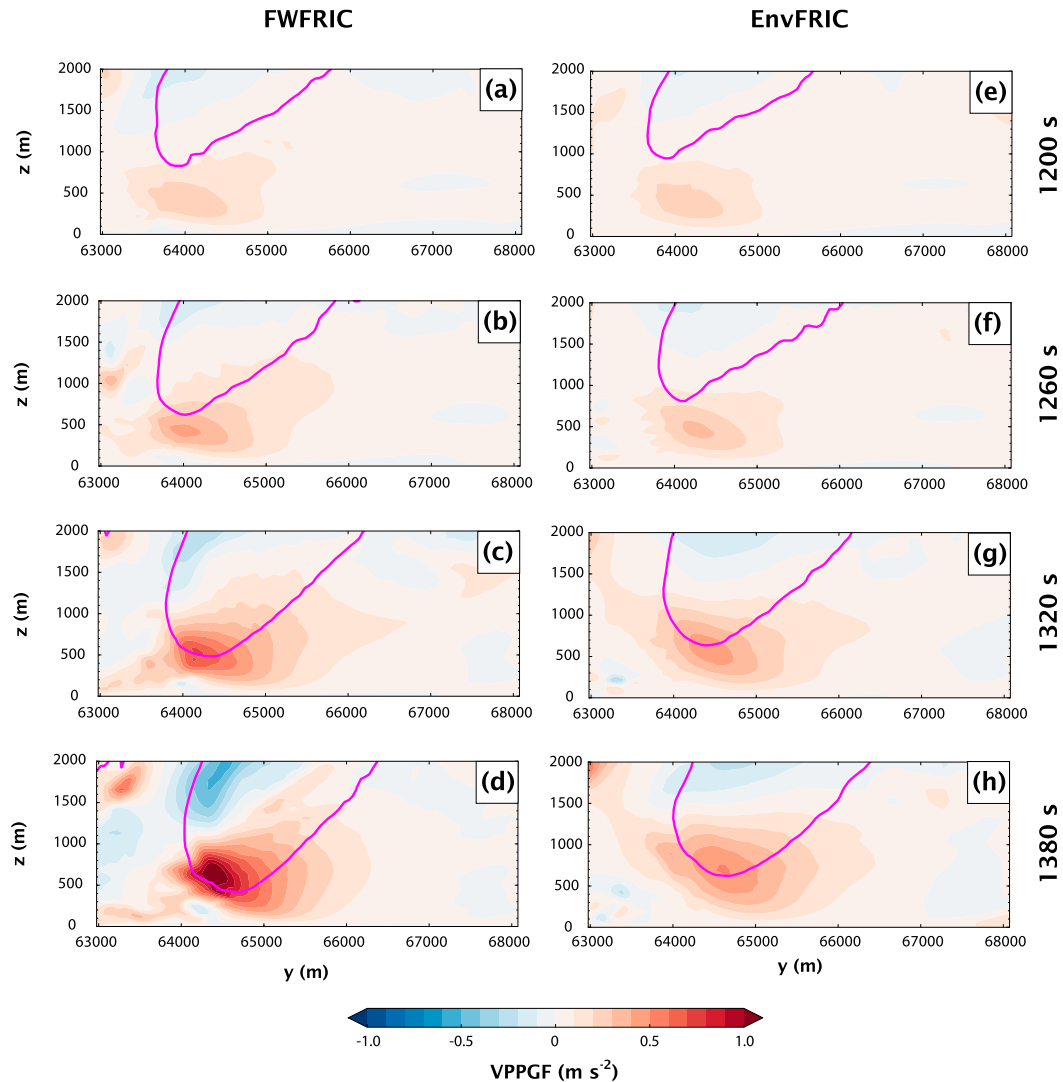


FIG. 4. As in Fig. 2, but the shaded quantity is the vertical perturbation pressure gradient force, and the magenta contour is the  $20 \text{ m s}^{-1}$  vertical velocity contour.

length in R16; in the present study, because we analyze material circuits consisting of many parcels, discarding those that pass below the lowest scalar level is impractical. Instead, we accept the uncertainty associated with the simplistic treatment below 10m AGL, while expecting that the resulting circulation budgets will still be qualitatively correct if the integrated circulation budgets agree well with model-predicted circulation values.

Figure 5a (Fig. 5d) presents an overview of circuits initialized in FWFRIC (EnvFRIC) around the mesocyclone at 500m AGL at 1320s. At this time, intensification of the low-level mesocyclone in FWFRIC has just begun. Over the preceding 10 min, circulation for the circuit in FWFRIC has increased by about 10%, with mixing accounting for most of the increase (Fig. 5b). Circulation about the circuit in EnvFRIC has

decreased by about 5% over the same period, with mixing again playing a more prominent role than baroclinic forcing (Fig. 5e). The mixing forcing term tends to be most positive (negative) in FWFRIC (EnvFRIC) from around 960–1200s, while the baroclinic term oscillates from positive to negative with a small net impact in both experiments (Figs. 5c and 5f). Overall, the change in circulation for these circuits is small in a relative sense, implying that most of the mesocyclone vorticity at 1320s is barotropic in origin.<sup>4</sup>

<sup>4</sup>This is true to the extent that circulation about the circuit at the beginning of the integration period is entirely barotropic; that is, that baroclinic and mixing forcing have not acted on the circuit during the very early part of the simulation. In reality, friction likely has contributed some small portion of this circulation.

## Mesocyclone, 1320 s at 500 m AGL

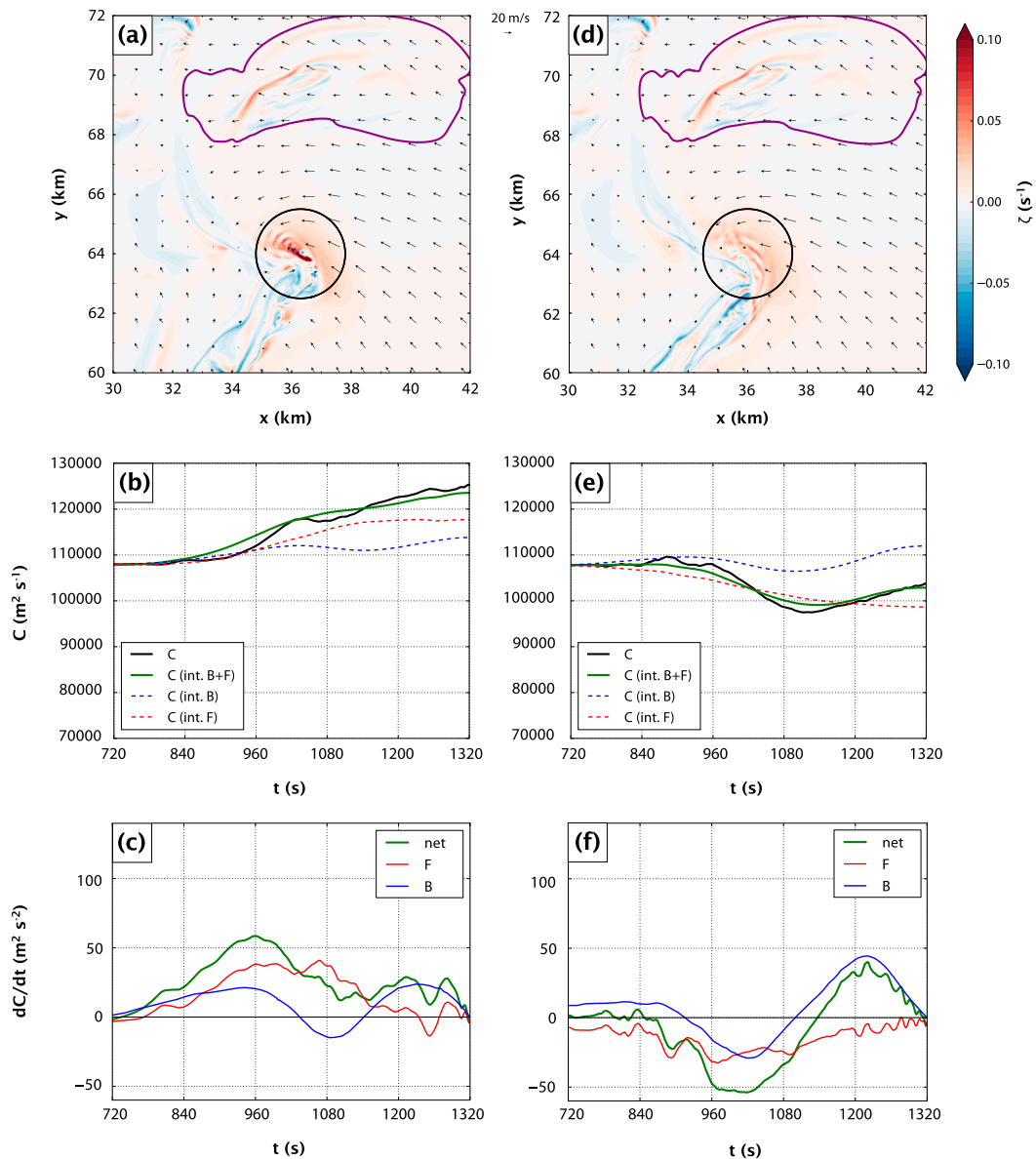


FIG. 5. Overview of material circuits initialized enclosing the mesocyclone at 500 m AGL and 1320 s. (top) Horizontal cross section of vertical vorticity (shaded), the  $0.3 \text{ g kg}^{-1}$  rainwater mixing ratio contour (purple), wind vectors, and the initial material circuit (black contour) at 1320 s and 500 m AGL in (a) FWFRIC and (d) EnvFRIC. (middle) Time series of circulation about the material circuit interpolated from model wind field (solid black), integrated from forcing terms (solid green), integrated from mixing forcing only (dashed red), and integrated from baroclinic forcing only (dashed blue) for (b) FWFRIC and (e) EnvFRIC. (bottom) Time series of circulation tendency owing to frictional forcing (red), baroclinic forcing (blue), and net forcing (green) for (c) FWFRIC and (f) EnvFRIC.

Figure 6a and Fig. 6d present an overview for analogous circuits at 500 m AGL but initialized at 1380 s. The cyclonic vorticity maxima inside the circuit in FWFRIC (Fig. 6a) have intensified relative to those initialized a minute earlier (Fig. 5a), indicative of the rapid low-level

mesocyclone intensification underway. The time series of circulation for the FWFRIC circuit (Fig. 6b) exhibits a dramatic change from that in Fig. 5b: circulation nearly doubles during the 10 min preceding the circuit initialization at 1380 s, and a large majority of this increase is

Mesocyclone, 1380 s at 500 m AGL

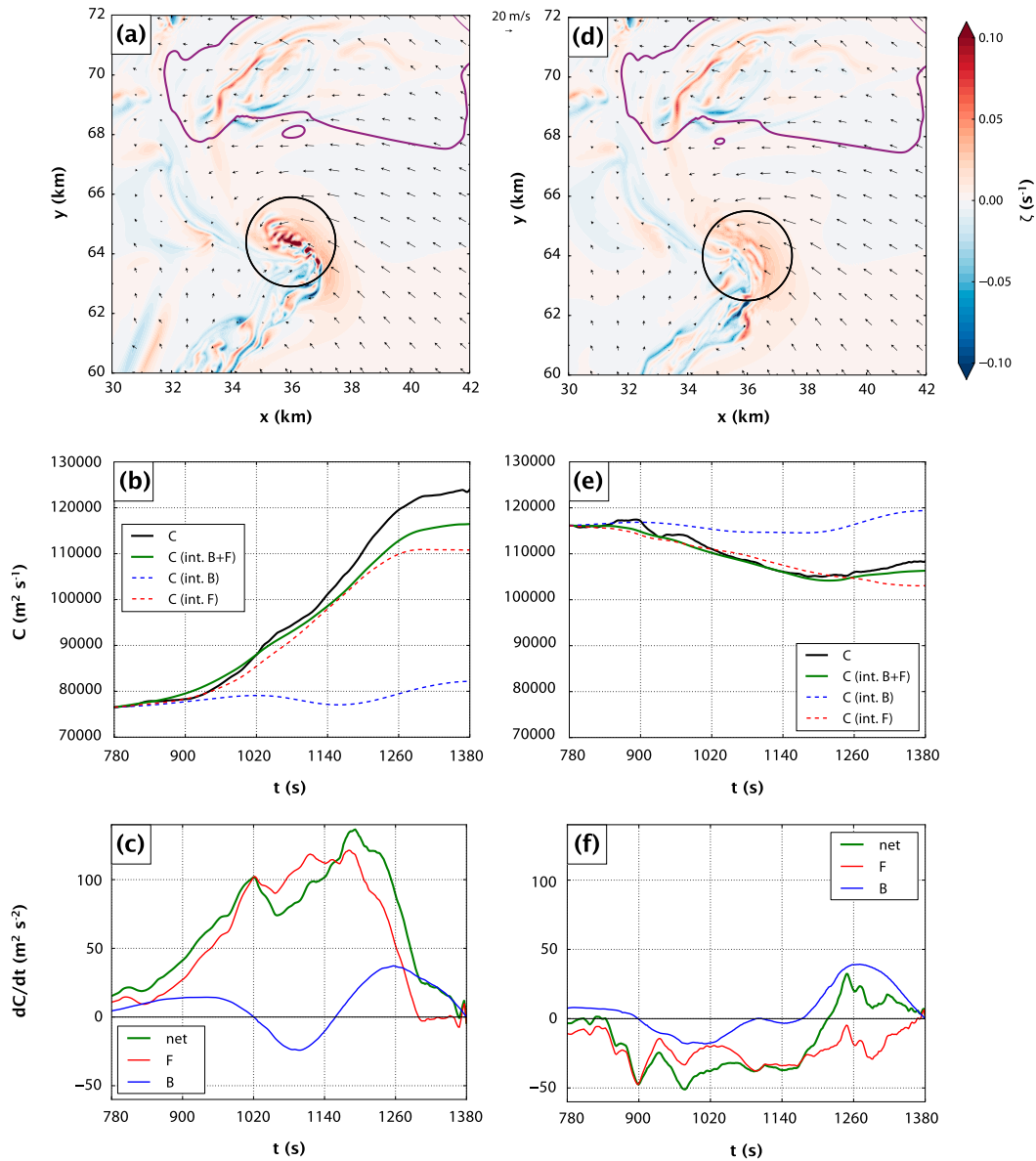


FIG. 6. As in Fig. 5, but for circuits initialized at 500 m AGL and 1380 s. The integration window begins at 780 s for these circuits.

due to mixing (Fig. 6c). For the circuit in EnvFRIC, the evolution of circulation is quite similar to the circuit initialized a minute earlier, with a small (<10%) decrease over the period owing primarily to mixing (Fig. 6e). A time series of the circulation forcing terms for the circuit in FWFRIC indicates that mixing forcing rapidly increases between 900 and 1020 s, then remains large and positive until 1260 s (Fig. 6c). As such, mixing augments circulation rapidly from about 6 to 2 min prior to the circuit reaching the periphery of the mesocyclone.

For EnvFRIC, the mixing term is once again weakly negative during this same period (Fig. 6f). In both simulations, baroclinic forcing again oscillates between weakly positive and negative values. Note that the final total circulation is quite similar for the FWFRIC circuits initialized at 1320 and 1380 s; we believe this can be reconciled with the mesocyclone intensification seen during the intervening period (cf. Figs. 2 and 4) through a process of mesocyclone contraction, wherein the peak values of cyclonic vorticity at 1380 s are

concentrated within a smaller area near the mesocyclone center.

The mixing term's relative contribution to the final value of circulation for the circuit in FWFRIC initialized at 1380 s is much larger ( $\sim 50\%$ ) than in the circuit initialized at 1320 s ( $\sim 10\%$ ). Between 1320 and 1380 s, the low-level mesocyclone also intensifies and lowers toward the ground. Thus, the introduction of large vorticity generated by surface drag via the mixing term<sup>5</sup> into the mesocyclone seems to be an important component in the intensification and lowering of the mesocyclone. Figure 7 displays time series of circuit parcel height distribution (below 1 km AGL) as heat maps. The circuit in FWFRIC initialized at 1320 s (Fig. 7a) contains a substantially smaller fraction of parcels lying below 40 m AGL throughout the integration period when compared with the circuit initialized at 1380 s (Fig. 7b). Physically, this implies that the low-level mesocyclone is drawing a larger proportion of its air from the near-ground layer at 1380 s than it had been a minute earlier at 1320 s; in turn, this allows surface drag to have a larger impact on the circuit at 1380 s. By contrast, when considering the circuits in EnvFRIC, the fraction of parcels in the lowest 40 m AGL remains similar for the circuits initialized at 1320 (Fig. 7c) and 1380 s (Fig. 7d). This result is more in line with the anemic mesocyclone intensification seen in EnvFRIC during this period.

To clarify the physical mechanisms driving this change in circulation, it is helpful to visualize the spatial evolution of the material circuit and the forcing terms along it. Note that in the following figures, we shade "forcing per unit length" along the circuit to illustrate where forcing terms are acting most prominently in a spatial sense. The quantities shaded in these figures are, for mixing and baroclinic forcing

$$\frac{\mathbf{F} \cdot d\mathbf{l}}{|d\mathbf{l}|} \quad \text{and} \quad (3)$$

$$\frac{B dz}{|d\mathbf{l}|}, \quad (4)$$

respectively, where  $\mathbf{F}$  and  $B$  are mean values along a line segment connecting two adjacent parcels along the circuit and  $|d\mathbf{l}|$  is the length of the line segment.

Figure 8 illustrates the evolution of the material circuit initialized around the mesocyclone at 500 m AGL in FWFRIC at 1320 s. At 960 s (6 min prior to the circuit's initialization), the western portion of the circuit extends upward to nearly 2000 m AGL in height and exhibits a

complex structure with many kinks. By contrast, the eastern half of the circuit contains large segments lying within the lowest 200 m AGL that feature only modest curvature, although the easternmost portion loops back upward to about 500 m AGL. At 1140 s, the circuit shape is qualitatively similar, although it has contracted slightly. Finally, at 1320 s, the circuit evolves into the circular shape we initialize it with at 500 m AGL. Circulation forcing from mixing remains relatively small in magnitude throughout the circuit's evolution, except for the vertical segments along its western extent. Here, diffusion within a region of compensating downdraft around the main storm updraft (not shown) tends to produce dipoles in the mixing term that largely offset one another (e.g., the forcing may be positive along portions of an "upward pointing" segment of the circuit, but there tends to be similar-magnitude negative forcing along the adjacent segment that descends from the circuit's summit). Thus, the net mixing forcing remains relatively small at all times. This pattern of dipoles with offsetting forcings along the higher portions of the circuit on its northwest flank is also seen with the baroclinic forcing term, as well.

Figure 9 illustrates the evolution for the circuit in FWFRIC initialized at 500 m AGL and at 1380 s, when rapid intensification of the low-level mesocyclone is underway. In terms of the shape and spatial distribution of the circuit, the evolution is qualitatively similar to the circuit in Fig. 8 that was initialized 1 min earlier, although we note that the total proportion of circuit lying very near the ground is larger for the circuit initialized at 1380 s (cf. Figs. 7a and 7b). Examination of the mixing term reveals a crucial difference for this later circuit: at 1020 and 1200 s, the forcing is large and positive for much of the segment that lies along the ground along the circuit's southern extent. This segment exists within the inflow region east of the low-level mesocyclone, an area of the storm where R16 also showed substantial crosswise vorticity generation by surface drag along tornado-entering parcel trajectories (e.g., their Fig. 16). As such, it is straightforward to interpret the physical meaning of the large positive mixing forcing on this segment of the circuit. The mixing term, under the influence of surface drag, represents a force directed toward the east. This force opposes the local westward-directed flow (i.e., inflow air accelerating into the mesocyclone to the west). Because the local flow here contributes negatively to circulation (i.e., it is locally consistent with clockwise flow about the circuit), a force retarding the flow actually contributes positively to total circulation about the circuit. This is simply a manifestation of the frictionally generated vorticity in the inflow region contributing to cyclonic vorticity in the low-level mesocyclone, much as

<sup>5</sup> The mixing term is large near ground because of the strong vertical gradient of the horizontal wind created by surface drag.

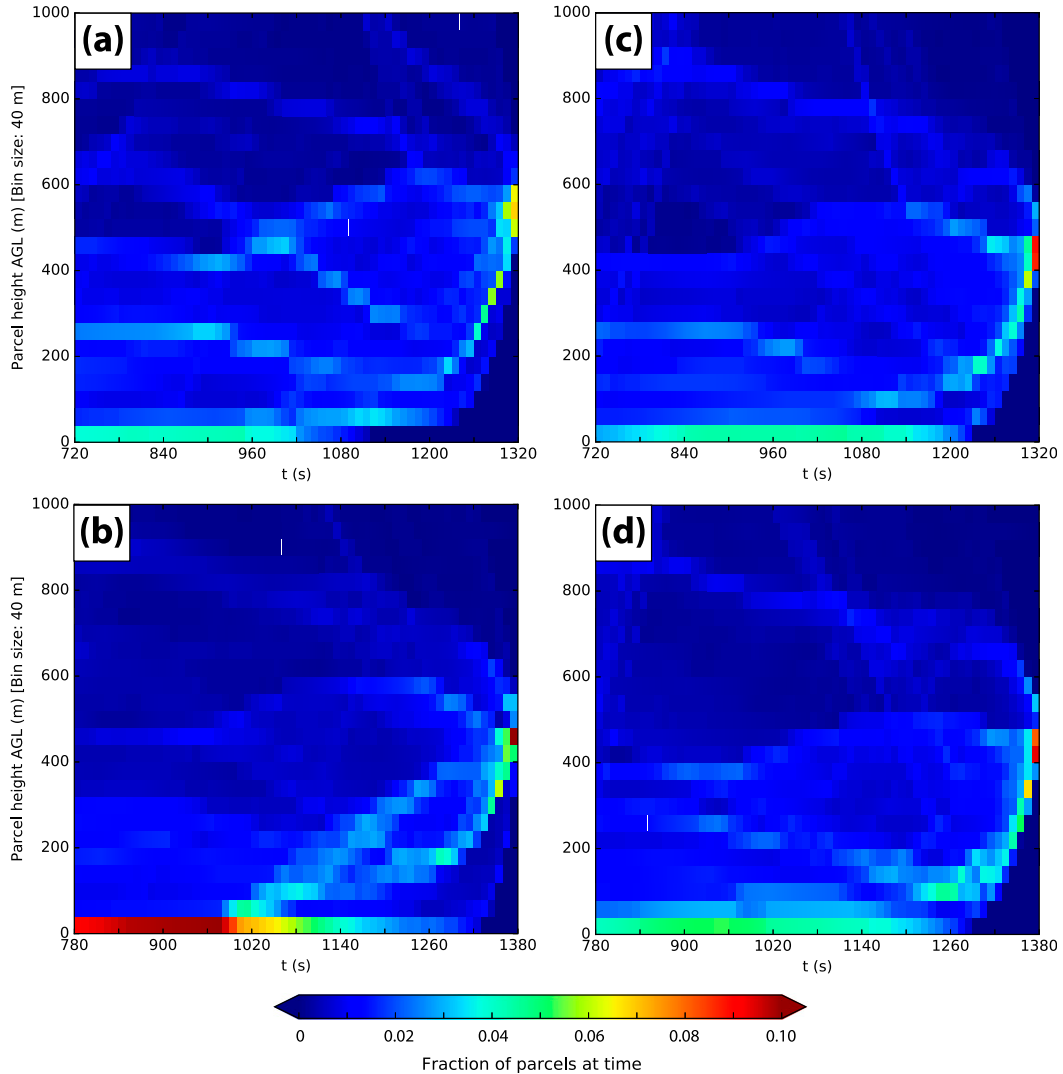


FIG. 7. Heat map of parcel height distribution over the integration period for the circuit initialized (a) in FWFRIC at 1320 s, (b) in FWFRIC as 1380 s, (c) in EnvFRIC at 1320 s, and (d) in EnvFRIC at 1380 s. The bins are 10 s along the abscissa and 40 m along the ordinate. In each bin, the shading represents the fraction of all parcels at that time that lie within the height bin (note that the total number of parcels comprising the circuit varies in time, so the shading does not correspond to an absolute number of parcels).

it contributed to the tornado’s vorticity for individual parcels analyzed in R16. For comparison, the evolution of the equivalent circuit (initialized at 500 m AGL, 1380 s) in EnvFRIC is presented in Fig. 10. While the spatial distribution of the circuit shares considerable similarity to that in Fig. 9, the main segment lying near the ground experiences weak negative mixing forcing at 1020 and 1200 s. This result implies generation of antistreamwise vorticity for parcels in this region, as predicted by M16 for the case of a free-slip lower boundary (see their Fig. 24): in the absence of surface drag (on the perturbation wind) that acts to create large vertical shear, the mixing mainly acts to reduce the

magnitude of vorticity extrema (in the case of EnvFRIC, it reduces the large barotropic streamwise vorticity in the inflow region).

To evaluate the contribution of frictionally generated vorticity for air parcels at other heights in the mesocyclone, additional circuits were initialized surrounding the mesocyclone at 1000 and 2000 m AGL in FWFRIC and EnvFRIC at the same times as the aforementioned circuits. Figure 11 presents circulation budgets for circuits initialized at 1320 s. In FWFRIC, the circuits at 500, 1000, and 2000 m AGL all experience a similar relative increase over the preceding 10 min (Fig. 11a), with both mixing and baroclinic forcing representing positive

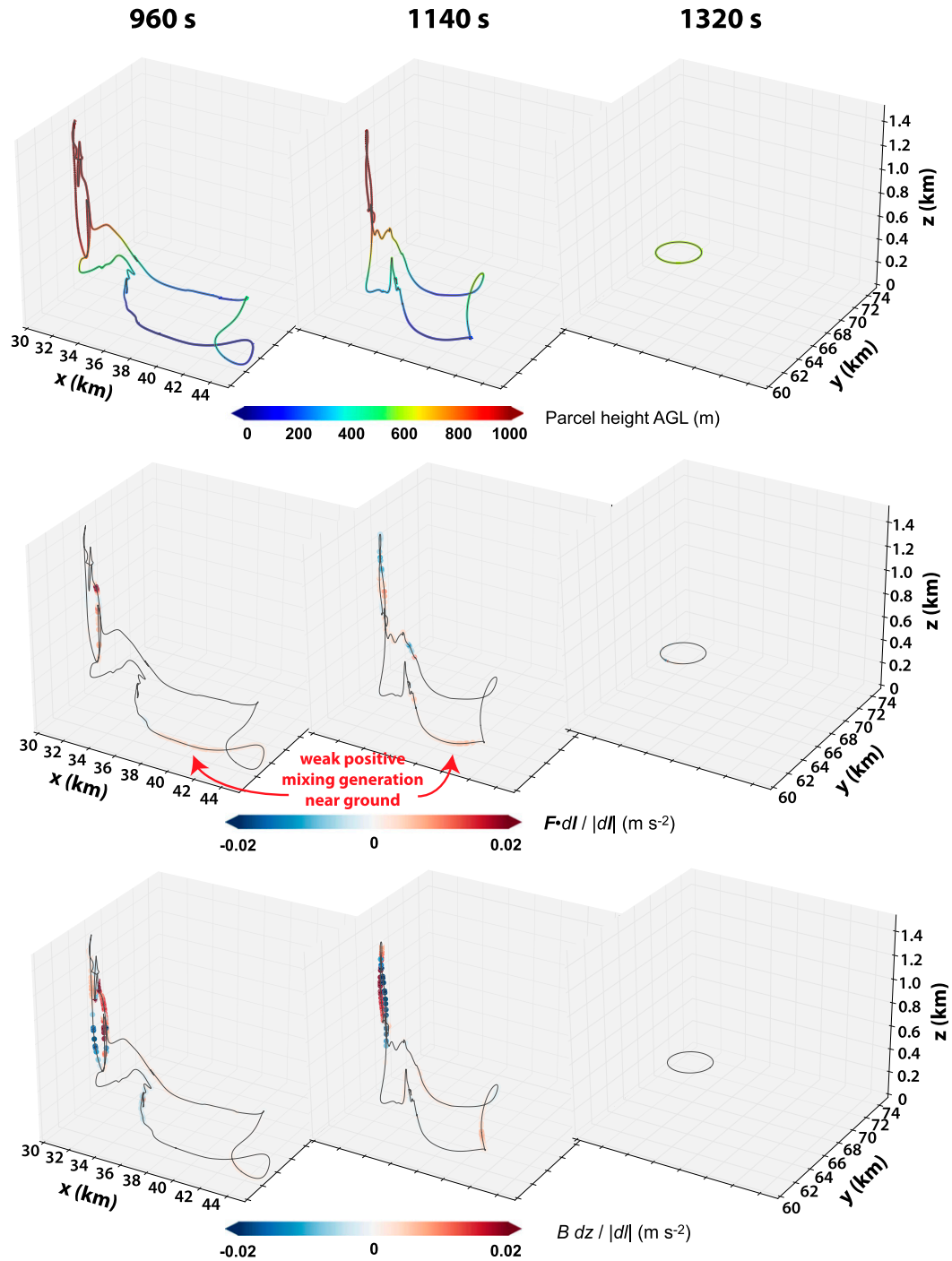


FIG. 8. Evolution of material circuit initialized at 1320 s around the low-level mesocyclone at 500 m AGL in FWFRIC. All panels represent the same circuit. (left)–(right) In each row, the panels progress forward in time according to the labels at the top of the figure, concluding with the circular circuit at 1320 s. (top) Parcels along the circuit are colored by height to help clarify the circuit’s 3D structure. (middle) Parcels are colored by  $\mathbf{F} \cdot d\mathbf{l}/|d\mathbf{l}|$  (the “mixing term”) for the adjacent circuit segment, which represents the local contribution to  $\oint \mathbf{F} \cdot d\mathbf{l}$  for that segment. (bottom) Parcels are colored by  $B dz/|d\mathbf{l}|$  (the “baroclinic term”), which represents the local contribution to  $\oint B dz$  for the adjacent circuit segment.

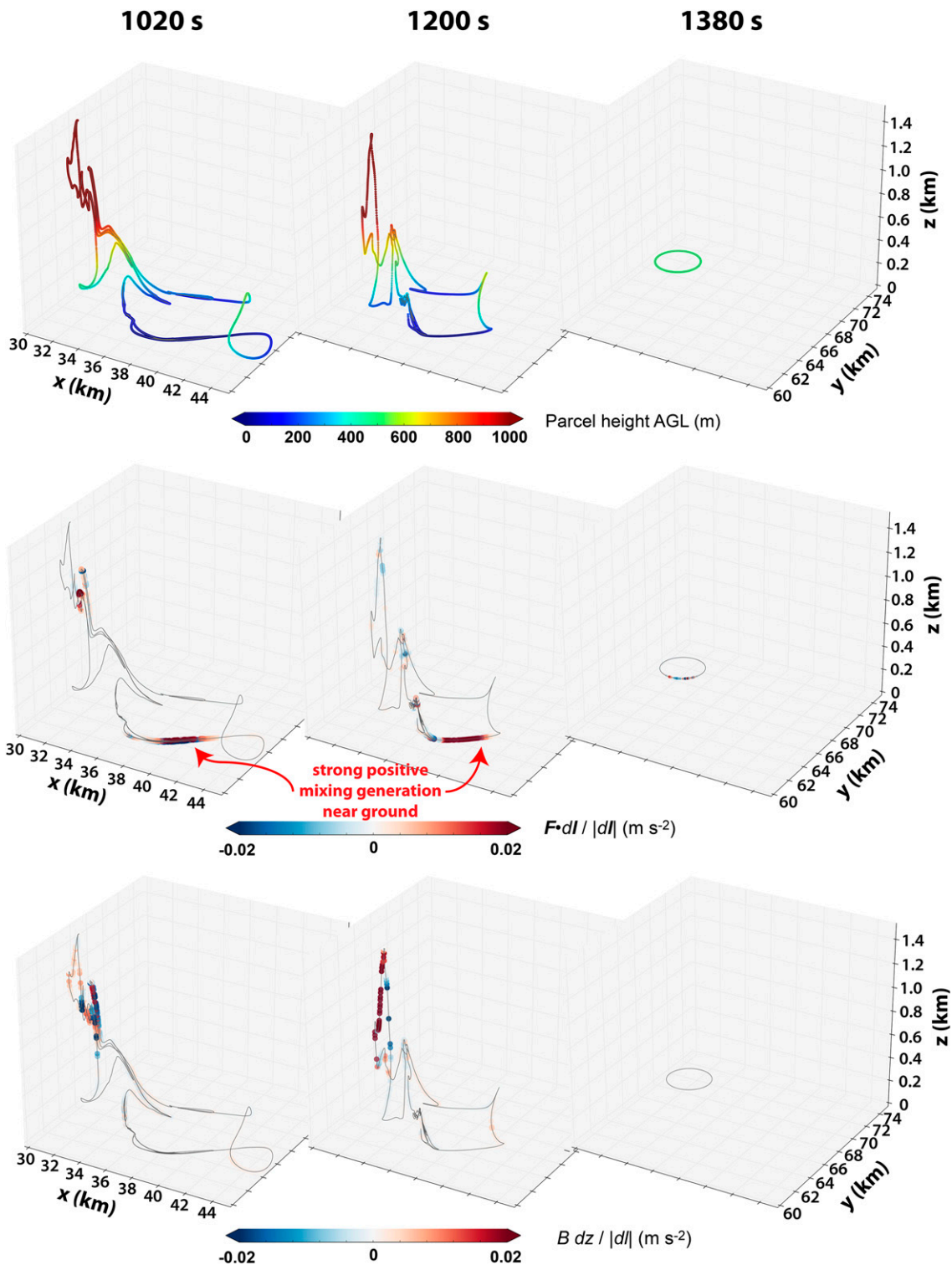


FIG. 9. As in Fig. 8, but for material circuit initialized around the low-level mesocyclone in FWFRIC at 500 m AGL at 1380 s.

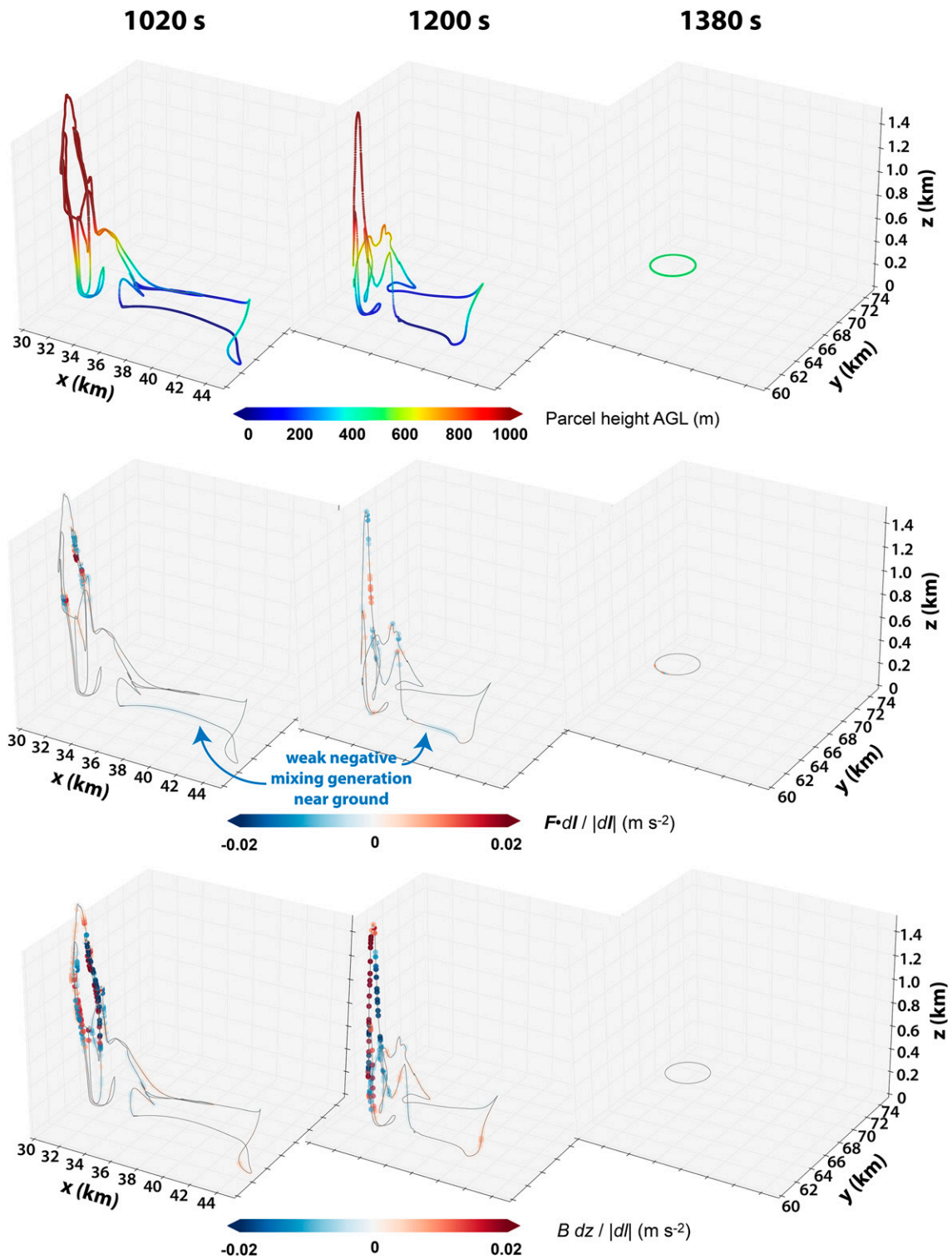


FIG. 10. As in Fig. 8, but for material circuit initialized around the low-level mesocyclone in EnvFRIC at 500 m AGL at 1380 s.

Mesocyclone, 1320 s

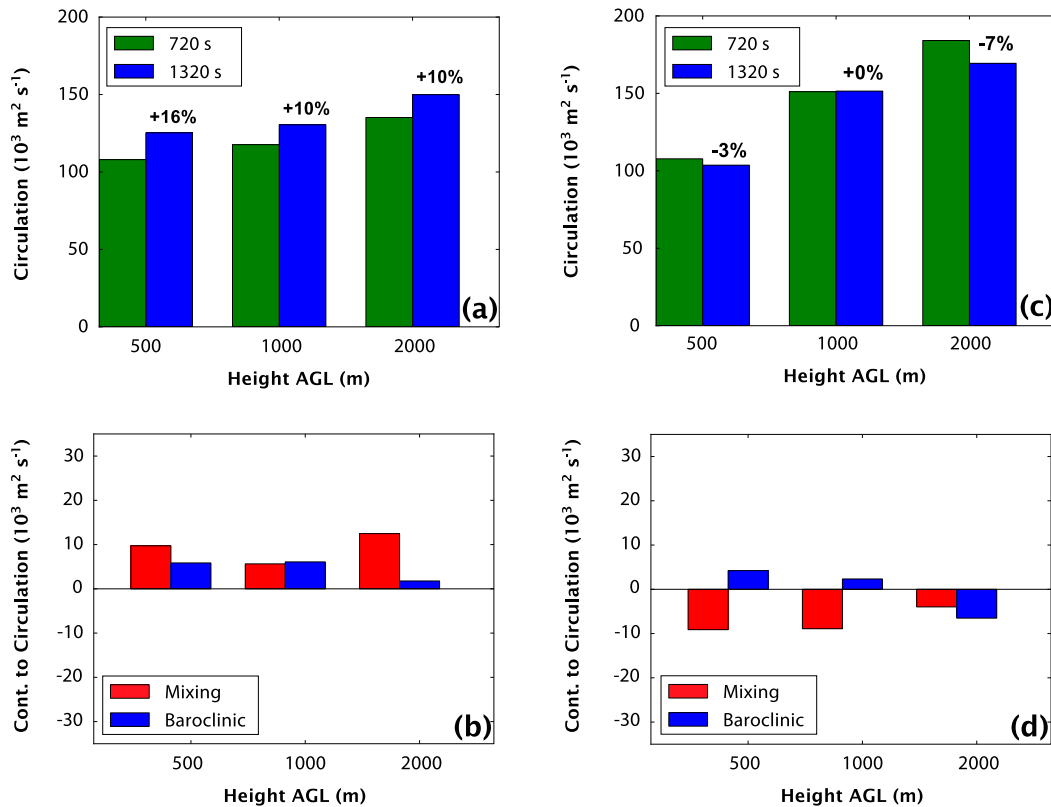


FIG. 11. (a) Circulation about the material circuits initialized at 1320 s in FWFRIC; values are presented at the beginning of the budget integration window (720 s; green) and the end of the window (1320 s; blue), and the percentage change over the period is given above the blue bar. These values are plotted for three separate circuits that were initialized surrounding the mesocyclone at 500, 1000, and 2000 m AGL. (b) Contribution to circulation from the mixing (red) and baroclinic (blue) forcing terms over the 10-min integration window for the same circuits in FWFRIC. (c) As in (a), but for the equivalent circuits in EnvFRIC. (d) As in (b), but for the equivalent circuits in EnvFRIC.

contributions (Fig. 11b). In EnvFRIC, the net changes in circulation over the preceding 10 min are relatively small for all heights (Fig. 11c), and the mixing force imposes small negative contributions in all cases (Fig. 11d).

Circulation budgets for circuits in FWFRIC initialized at 1380 s tell a much different story: the relative increase in circulation over the preceding 10 min is much larger at 500 m AGL (62%) than at 1000 (28%) and 2000 m AGL (14%) (Fig. 12a). This discrepancy with height owes

primarily to the mixing term, whose integrated contribution becomes progressively smaller with height<sup>6</sup> (Fig. 12b). Because the lowering of the mesocyclone in FWFRIC seems to be a crucial difference relative to EnvFRIC immediately preceding tornadogenesis in the former, these circulation budgets further implicate frictional vorticity: at 500 m AGL, where the mesocyclone is much stronger in FWFRIC than EnvFRIC by 1380 s, the frictional contribution is substantially larger than at 1000–2000 m AGL. These results indicate that the contribution of frictionally generated vorticity is large for parcels entering the low-level mesocyclone in FWFRIC. It should be noted that while baroclinic forcing plays a much smaller role, it is still a non-negligible secondary positive contribution to the final circulation at 500 and 1000 m AGL. For the circuits in EnvFRIC at 1380 s (Figs. 12c and 12d), the budgets at all heights are qualitatively similar to those at 1320 s,

<sup>6</sup>The discrepancy in the mixing contribution over the 10 min integration window does not represent all generation that has occurred along the circuit since the beginning of the simulation; it is possible that the circuits initialized at 1000 and 2000 m AGL experienced some mixing generation as a result of surface drag before the integration time window. However, earlier in the simulation, the storm-induced ground-relative perturbation wind tends to be weak; thus, frictional vorticity generation should be modest.

## Mesocyclone, 1380 s

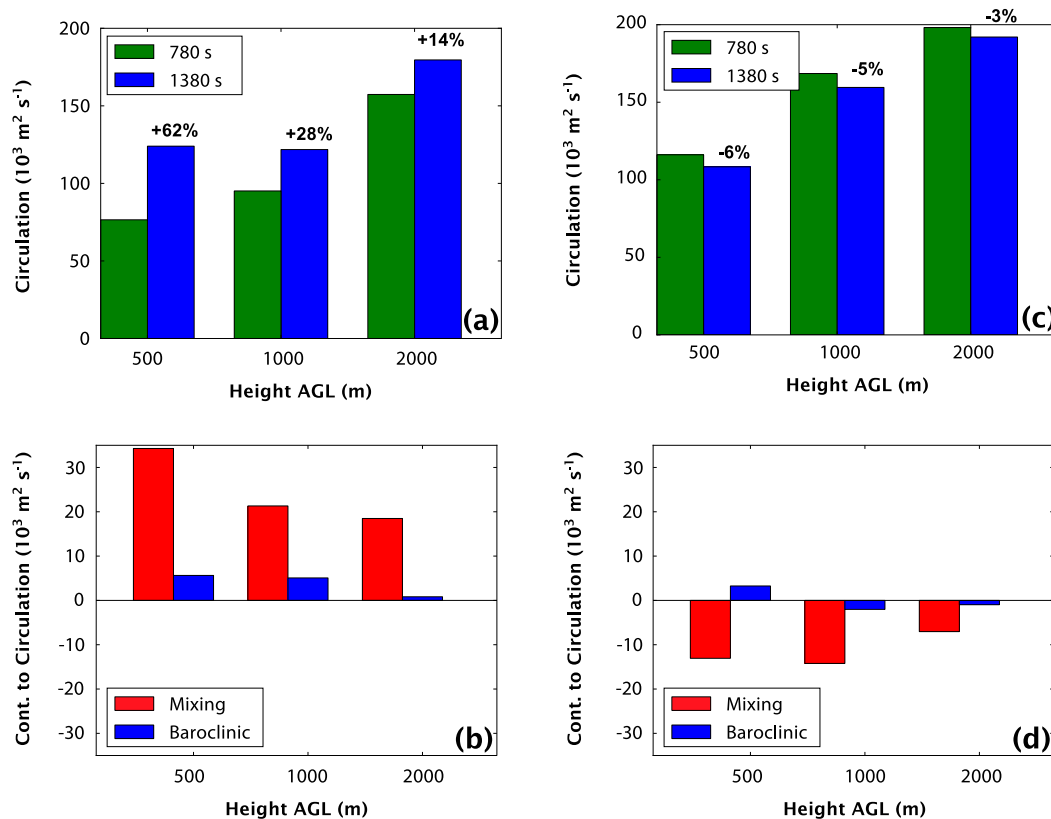


FIG. 12. As in Fig. 11, but for circuits initialized at 1380 s. The beginning of the budget integration window for these circuits is 780 s.

mirroring the relatively steady intensity of the mesocyclone over the interim period.

### c. Circulation analyses of material circuits enclosing the tornado in FWFRIC

The circulation analyses presented above have established the important role of surface drag acting on the storm-induced flow for the intensification of the low-level mesocyclone that precedes tornadogenesis in FWFRIC. In R16, only trajectory-based vorticity budget analyses were performed. To clarify the results of R16 and increase their robustness, we apply the same circulation analysis techniques to the incipient tornado in FWFRIC. In this case, horizontal, circular material circuits of radius 1.5 km are initialized at six heights—100, 200, 400, 600, 800, and 1000 m AGL—enclosing the incipient tornado at 1500 s. The 1.5-km radius, which was again chosen to keep circuit parcels away from strong wind gradients that greatly reduce the accuracy of trajectory calculations, encloses portions of the low-level mesocyclone immediately surrounding the tornado vortex; therefore, changes in circulation for these

circuits may not always directly correspond to the evolution of vertical vorticity within the tornado itself. However, most of the circulation change over the budget period should be related to the rapidly strengthening tornado vortex centered within the mesocyclone; this is particularly true because of the strongly convergent wind field, which tends to contract the circuits quickly toward the vortex center when integrated forward in time (not shown).

Figure 13a compares the total circulation of these circuits 10 min prior to initialization (900 s) with the values at initialization (1500 s); this is the same integration window used for trajectories in R16 that were initialized within the tornado at 1500 s. A clear, stable trend is evident wherein the relative increase in circulation over the 10 min preceding tornadogenesis is larger at lower heights. Circulation more than doubles over this period for the circuit initialized at 100 m AGL, while it increases by only 26% for the circuit at 1000 m AGL.

Figure 13b presents the integrated contributions to circulation over the preceding 10 min by the mixing and baroclinic forcing terms for the same circuits in Fig. 13a.

### Tornado, 1500 s

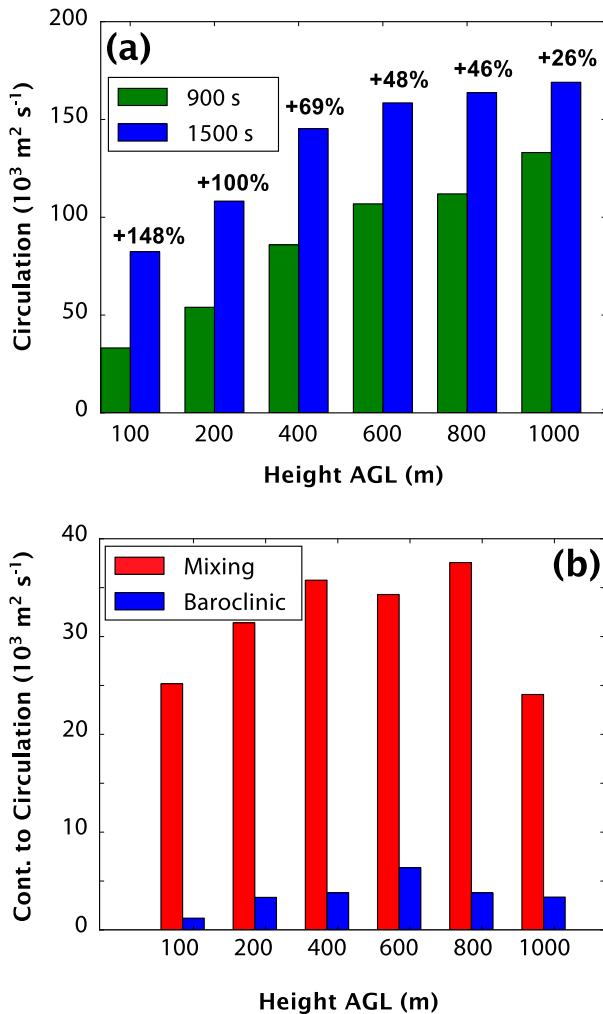


FIG. 13. (a) Circulation about material circuits initialized at six heights enclosing the incipient tornado in FWFRIC at 1500 s; values are presented at the beginning (900 s; green) and end (1500 s; blue) of the budget integration window, and the relative change over the period is given above each blue bar. (b) Contribution to circulation from the mixing (red) and baroclinic (blue) forcing terms over the 10-min integration window for the same circuits.

The contribution from mixing is approximately an order of magnitude larger than baroclinicity for all circuit initialization heights in the tornado. As such, the increases in circulation between 900 and 1500 s seen in Fig. 13a owe primarily to surface drag.

The dominance of frictional forcing in the circulation budgets for the tornado-enclosing circuits bolsters confidence in the narrative presented in R16 (cf. their Figs. 12 and 14), particularly regarding what we termed therein as mechanism II (the import of frictionally generated vorticity into the incipient tornado). A chief concern regarding the trajectory analysis in R16 was the

limitation imposed by poor vorticity budget accuracy when parcels descended below the lowest scalar level (10 m AGL). This limitation forced us to exclude these parcels from our analysis, in effect placing a lower bound of about 400 m AGL on the height at which we could initialize trajectories in the tornado (trajectories initialized any lower tended to originate almost exclusively from below 10 m AGL). Thus, while we demonstrated conclusively that frictional vorticity was an important source of tornadic vorticity at 400 m AGL, a degree of speculative extrapolation was necessary in R16 to invoke this same mechanism near the ground. With the circulation analyses performed in the present study, frictional vorticity is clearly shown to play a crucial role in the tornado below 400 m AGL; in fact, its role is increasingly larger with decreasing height down to at least 100 m AGL, as a fraction of total circulation. We are therefore much more confident that in FWFRIC, vorticity near the ground in the incipient tornado at 1500 s is overwhelmingly frictional in origin. The circulation analyses also show that the contribution of frictionally generated vorticity within the incipient tornado is greater than for the preceding low-level mesocyclone; this appears to be a consequence of most air parcels entering the tornadic region originating from very near the ground, allowing surface drag to modify their vorticity over an extended duration.

Circuits are also initialized enclosing the strengthening tornado at 1560 s, but the circulation budgets are much less reliable and some circuits became excessively distorted only 5–7 min into the backward integration (not shown). In general, the source terms for circulation tendency along these circuits initialized at 1560 s suggest a somewhat greater role for baroclinic generation than for the circuits initialized at 1500 s, although frictional generation remains the largest contributor. This is in line with the theoretical arguments of Dahl (2015) as well as the simulation results of MS16b, which suggest the relative importance of baroclinic vorticity becomes greater as a tornado matures.

#### d. Near-ground vertical wind shear in the inflow region

MB16 raised concerns pertaining to the potential overestimation of near-ground wind shear in laminar flows for LESs, which was shown to be quite severe for their idealized case initialized with a background wind profile that was constant with height. We wish briefly to address the potential applicability of this issue to our simulations herein. It is important to emphasize that the original sounding (MAY3) extracted from a real-data simulation had already been subject to parameterized PBL mixing and is further spun up through 48 h of a 1D column simulation that includes surface friction to reach a

steady state three-force balance. Therefore, our environmental profile should not suffer from the problem highlighted in MB16, which depicted a “worst-case scenario” where the model was forced to develop a PBL wind profile from an (unrealistic) initial profile with zero vertical shear. Thus, in our experiments, we do not expect the type of extreme near-ground shear overestimation seen in MB16.

In our experiment FWFRIC, the storm-induced flow is subject to surface drag. This means when the low-level inflow accelerates toward the storm, near-surface shear should increase. It is worthwhile to evaluate the magnitude of this increase to ensure it is physically reasonable. As a reference point, we look to Nowotarski and Markowski (2016, hereafter NM16), who examined supercell simulations at 200-m horizontal grid spacing; unlike our simulations, they perturbed the initial PBL flow to induce the development of boundary layer eddies and rolls in the storm environment. Their simulations also included surface heating due to radiation. As such, their simulations should not be subject to the concerns raised in MB16. They found that the 0–1-km SRH calculated from a mean profile in their near-storm inflow environment exceeded that in the far field by as much as 78% for experiments with convective rolls primarily perpendicular to the storm motion (see their Fig. 3 and Table 1). In Fig. 14a, we present a comparison of the MAY3B hodograph used to initialize our experiments against an average “near storm” inflow profile in FWFRIC at 1080 s (during the time period in which we show important effects from surface drag in our circulation budgets). Figure 14b shows the spatial context of this average profile within a horizontal cross section at 10 m AGL, including the position of the circuit from Fig. 6 at that time. The 0–1-km SRH in our averaged inflow profile is approximately 79% larger than in MAY3B. The enhancement to the 0–1-km SRH by surface drag in our near-storm environment (79%) is almost identical in magnitude to the perpendicular-roll CBL simulations of NM16 (78%), even though we do not explicitly introduce thermal perturbations to promote convective eddies and rolls within the boundary layer. In fact, even if we were to introduce such perturbations, we would not expect development of significant resolvable eddies in our simulations because no surface radiative heating is included (as in NM16’s CBL experiments). The SGS turbulence mixing in our simulations is playing the role of shear-induced eddy mixing and keeping the resolved flow more or less laminar outside the storm.

#### 4. Summary and discussions

In this study, the low-level mesocyclone evolution was examined in two supercell simulations differentiated solely

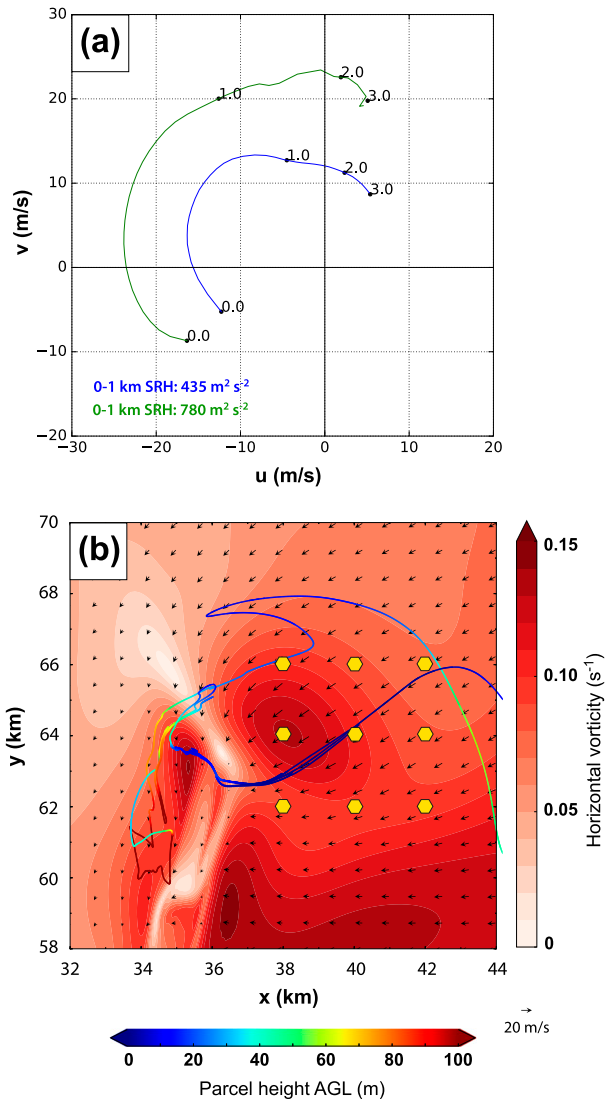


FIG. 14. (a) Comparison of hodographs for the initial sounding MAY3B (blue), and an average of nine points in the inflow region in FWFRIC at 1080 s (green). (b) Horizontal cross section at 10 m AGL in FWFRIC at 1080 s of horizontal vorticity (shaded) and wind vectors. The nine yellow hexagons denote points from which the averaged “near storm” hodograph in (a) is derived. The position at 1080 s for the circuit from Fig. 6 is overlaid for context, colored by the local parcel height AGL.

by how the surface drag is applied. In the simulation with drag applied to the full wind (FWFRIC), the mesocyclone rapidly intensified and lowered below 1 km AGL between 1200 and 1500 s, leading to tornadogenesis; in the simulation with drag applied only to the base-state wind (EnvFRIC), the mesocyclone only intensified and lowered modestly during this period, and tornadogenesis did not occur.

Rapid intensification of the low-level mesocyclone in FWFRIC appears to have its origins in the stronger

horizontal convergence along the storm-scale convergence boundary at the surface (relative to EnvFRIC), which promotes a modestly stronger low-level updraft from 1200 to 1320 s and, hence, stronger stretching of environmental vorticity after it is tilted into the vertical. Once vorticity within the low-level mesocyclone begins to ramp up during this period, the corresponding dynamic pressure drop yields an enhanced upward-directed VPPGF below 1 km AGL and initiates a positive feedback cycle of intensification and lowering of the mesocyclone. The presence of large frictionally generated vorticity in the inflow region east of the convergence boundary in FWFRIC is a key factor that sustains this cycle for several minutes, culminating in tornadogenesis by 1500 s. In EnvFRIC, relatively weaker convergence at the surface (and associated low-level updraft) hampers the establishment of this feedback cycle. Furthermore, even to the limited extent that the feedback does occur in EnvFRIC, the lack of frictionally enhanced horizontal vorticity for parcels near the ground further inhibits its progression relative to FWFRIC.

Leslie (1971) proposed a mechanism by which a vortex may build downward with time through a bootstrap process known as the dynamic pipe effect (DPE), and this idea has influenced the subsequent literature on tornadogenesis. The positive feedback observed during the low-level mesocyclone intensification and lowering in FWFRIC shares some similarities with the DPE. Trapp and Davies-Jones (1997) used analytical and numerical models to illustrate a theoretical basis for the role of the DPE in real-world tornadogenesis. Davies-Jones et al. (2001), however, argued against the DPE as a mechanism capable of generating a vortex at the ground from purely barotropic vorticity; in other words, the midlevel mesocyclone formed from tilting environmental vorticity probably cannot build all the way to the ground simply through the bootstrap process. Nonetheless, the DPE can potentially explain the lowering of a mesocyclone below 1 km AGL, particularly in cases where horizontal streamwise vorticity is very large at the time it is tilted into the vertical. Wicker and Wilhelmson (1995) and Noda and Niino (2010) noted dynamically induced lowering of low-level mesocyclones similar to that in FWFRIC herein; in their simulations, baroclinic vorticity provided the surplus of horizontal vorticity near the ground necessary for rapid vortex stretching below 1 km AGL.

The circulation analyses we presented for FWFRIC during mesocyclone intensification show that frictional circulation is generated rapidly on segments of the circuit lying near the ground in the inflow region. A conceptualized illustration of this circuit evolution is presented in Fig. 15a, with an annotated zoom of the drag-induced circulation generation region in Fig. 15b.

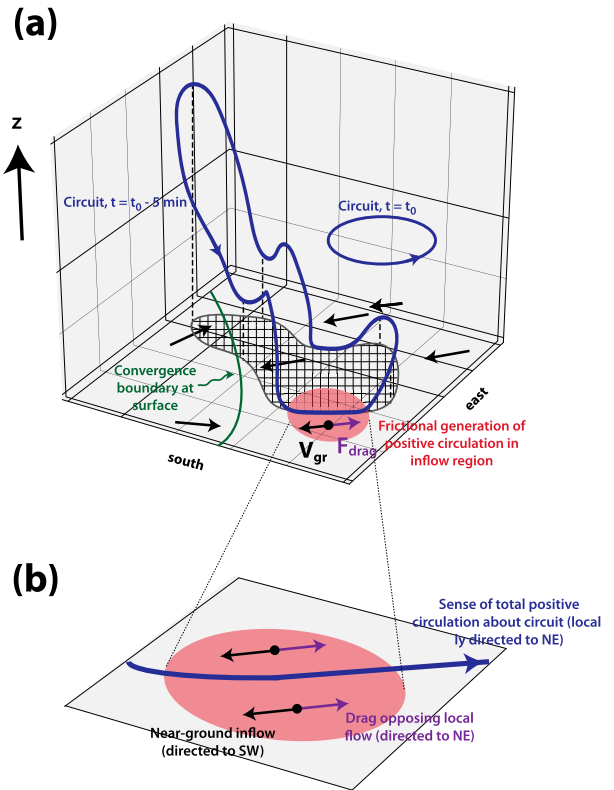


FIG. 15. (a) Conceptual model for evolution of a circuit that encloses the low-level mesocyclone in FWFRIC during rapid intensification. The partial cube in the background (light gray with gridlines) is viewed from above and the southeast, with walls drawn on its bottom, western, and northern faces. The circuit is denoted by a blue curve with snapshots shown at two different times:  $t = t_0$  and  $t = t_0 - 5$  min. The blue arrows along the circuit indicate the sense of total circulation. The hatched region enclosed in a heavy gray line is the horizontal projection of the circuit at  $t = t_0 - 5$  min onto the ground. The southeastern portion of the circuit at this time descends below 100 m AGL, where a northeastward-directed frictional force generates large positive circulation tendency; the area containing the circuit segment where this occurs is shaded in red. The horizontal ground-relative wind at 10 m AGL is given by black vectors, while the frictional force at 10 m AGL is given by the purple vector. The green curve denotes the position of the convergence boundary at 10 m AGL, which is located south and west of the main frictional generation zone. (b) Zoomed view of the red circle in (a), which lies in a horizontal plane at approximately 10 m AGL. Vectors and blue curve are as in (a), but annotated to clarify the physical processes and emphasize that the drag force and circuit circulation are both directed toward the northeast in this area.

Note that the convergence boundary is simply a near-ground wind-shift line bisecting the low-level mesocyclone, separating generally westward-directed (to the northeast of the boundary) and eastward-directed (to the southwest of the boundary) flows (cf. Fig. 6a). When parcels are drawn upward into the low-level mesocyclone from the inflow region east of the boundary (e.g., the red zone along

the ground in Figs. 15a and 15b) and their horizontal vorticity is tilted into the vertical, the large frictionally generated vorticity component gives them a “head start” in cyclonic vorticity amplification, relative to near-ground parcels drawn into the mesocyclone in EnvFRIC. The initial horizontal vorticity of the near-ground parcels in EnvFRIC is approximately limited to that of the background environment, as drag has not acted to enhance vorticity within the inflow region in that experiment. Bluestein (2007) argues that low-precipitation supercells, owing to their lack of strong cold pools, should not be expected to produce strong low-level mesocyclones “unless there is strong, pre-existing horizontal vorticity in the boundary layer” (p. 1285). During the early stages of our simulated storm in the present study, the storm shares thermodynamic characteristics with a low-precipitation supercell, so similar logic applies. While the background shear in the sounding used for both of our experiments features considerable vorticity in the boundary layer (e.g., 0–1-km SRH of  $435 \text{ m}^2 \text{ s}^{-2}$ ), the substantial enhancement of vorticity by drag within the lowest few hundred meters AGL in FWRIC appears to tip the scale in favor of rapid mesocyclogenesis down to 400 m AGL.

Although our results are robust in terms of the signal in the circulation budgets, as well as the agreement between the interpolated (from model-predicted fields) and integrated values of circulation in the budgets, there are a couple of caveats that bear reiterating. First, our treatment of circuit parcels passing below 10 m AGL introduces a certain degree of uncertainty (there are no grid levels below 10 m AGL to resolve the near-wall gradient of flow). Second, LES turbulence schemes tend to overestimate near-wall shear of wall-parallel flows, which may quantitatively affect the amount of vorticity generation by the surface drag. We again note that this problem is different from the shear overestimation problem specific to laminar flow in LES discussed in MB16; in our case, the inflow profile comes from a background sounding already subject to the effects of surface drag and is in a three-force balance.

Our analysis of circuits enclosing the incipient tornado at 1500 s in FWRIC corroborates the critical role of frictionally generated vorticity that we proposed in R16. Furthermore, the circulation budgets for these circuits quantitatively demonstrate an unsurprising but important fact: within the lowest 1 km AGL of the tornado, frictional forcing accounts for a decreasing proportion of the total circulation with height. At 100 m AGL, more than half of the total circulation surrounding the tornado at 1500 s owes directly to friction. This suggests that despite the large barotropic vorticity in this layer from the background wind shear, new vorticity generated by friction within accelerating inflow during the 5–8 min prior to tornadogenesis can

be the most important source of tornadic vorticity near the ground. In future work, we plan to investigate this phenomenon by applying circulation budget analysis to a wider array of simulations, including those with heterogeneous initial conditions and tornadoes that occur in the presence of an established cold pool. We also plan to perform additional idealized simulations with different sounding profiles and different drag coefficients, which should help to clarify how generalizable the conclusions of R16 and the present study are for tornadic storms.

*Acknowledgments.* This work was primarily supported by NSF Grant AGS-0802888. The second author was also supported by NSF Grants AGS-1046171 and AGS-1261776. Numerical simulations were performed at the Texas Advanced Supercomputing Center, an NSF XSEDE facility. The authors wish to thank Drs. Daniel Dawson and Alex Schenkman for their helpful discussions during the early stages of this work. We also thank Dr. Dawson for providing a sounding profile extracted from his earlier simulation of the 3 May 1999 outbreak. Finally, thorough critiques by Dr. Lou Wicker and two other anonymous reviewers were invaluable, resulting in significant improvements to the manuscript; we thank them for their time and efforts.

## REFERENCES

- Bluestein, H. B., 2007: Advances in applications of the physics of fluids to severe weather systems. *Rep. Prog. Phys.*, **70**, 1259–1323, doi:10.1088/0034-4885/70/8/R01.
- Chow, F. K., R. L. Street, M. Xue, and J. H. Ferziger, 2005: Explicit filtering and reconstruction turbulence modeling for large-eddy simulation of neutral boundary layer flow. *J. Atmos. Sci.*, **62**, 2058–2077, doi:10.1175/JAS3456.1.
- Dahl, J. M. L., 2015: Near-ground rotation in simulated supercells: On the robustness of the baroclinic mechanism. *Mon. Wea. Rev.*, **143**, 4929–4942, doi:10.1175/MWR-D-15-0115.1.
- Davies-Jones, R., 1984: Streamwise vorticity: The origin of updraft rotation in supercell storms. *J. Atmos. Sci.*, **41**, 2991–3006, doi:10.1175/1520-0469(1984)041<2991:SVTOOU>2.0.CO;2.
- , R. J. Trapp, and H. B. Bluestein, 2001: Tornadoes and tornadic storms. *Severe Convective Storms, Meteor. Monogr.*, No. 50, Amer. Meteor. Soc., 167–221.
- Dawson, D. T., II, M. Xue, J. A. Milbrandt, and M. K. Yau, 2010: Comparison of evaporation and cold pool development between single-moment and multimoment bulk microphysics schemes in idealized simulations of tornadic thunderstorms. *Mon. Wea. Rev.*, **138**, 1152–1171, doi:10.1175/2009MWR2956.1.
- , —, —, and A. Shapiro, 2015: Sensitivity of real-data simulations of the 3 May 1999 Oklahoma City tornadic supercell and associated tornadoes to multimoment microphysics. Part I: Storm- and tornado-scale numerical forecasts. *Mon. Wea. Rev.*, **143**, 2241–2265, doi:10.1175/MWR-D-14-00279.1.
- Grasso, L. D., and W. R. Cotton, 1995: Numerical simulation of a tornado vortex. *J. Atmos. Sci.*, **52**, 1192–1203, doi:10.1175/1520-0469(1995)052<1192:NSOATV>2.0.CO;2.

- Lee, B. D., C. A. Finley, and C. D. Karstens, 2012: The Bowdle, South Dakota, cyclic tornadic supercell of 22 May 2010: Surface analysis of rear-flank downdraft evolution and multiple internal surges. *Mon. Wea. Rev.*, **140**, 3419–3441, doi:10.1175/MWR-D-11-00351.1.
- Lemon, L. R., and C. A. Doswell, 1979: Severe thunderstorm evolution and mesocyclone structure as related to tornadogenesis. *Mon. Wea. Rev.*, **107**, 1184–1197, doi:10.1175/1520-0493(1979)107<1184:STEAMS>2.0.CO;2.
- Leslie, L. M., 1971: The development of concentrated vortices: A numerical study. *J. Fluid Mech.*, **48**, 1–21, doi:10.1017/S0022112071001435.
- Markowski, P. M., 2016: An idealized numerical simulation investigation of the effects of surface drag on the development of near-surface vertical vorticity in supercell thunderstorms. *J. Atmos. Sci.*, **73**, 4349–4385, doi:10.1175/JAS-D-16-0150.1.
- , and Y. P. Richardson, 2014: The influence of environmental low-level shear and cold pools on tornadogenesis: Insights from idealized simulations. *J. Atmos. Sci.*, **71**, 243–275, doi:10.1175/JAS-D-13-0159.1.
- , and G. H. Bryan, 2016: LES of laminar flow in the PBL: A potential problem for convective storm simulations. *Mon. Wea. Rev.*, **144**, 1841–1850, doi:10.1175/MWR-D-15-0439.1.
- , E. N. Rasmussen, and J. M. Straka, 1998: The occurrence of tornadoes in supercells interacting with boundaries during VORTEX-95. *Wea. Forecasting*, **13**, 852–859, doi:10.1175/1520-0434(1998)013<0852:TOOTIS>2.0.CO;2.
- Marquis, J., Y. Richardson, P. Markowski, D. Dowell, and J. Wurman, 2012: Tornado maintenance investigated with high-resolution dual-Doppler and EnKF analysis. *Mon. Wea. Rev.*, **140**, 3–27, doi:10.1175/MWR-D-11-00025.1.
- Mashiko, W., 2016a: A numerical study of the 6 May 2012 Tsukuba City supercell tornado. Part I: Vorticity sources of low-level and midlevel mesocyclones. *Mon. Wea. Rev.*, **144**, 1069–1092, doi:10.1175/MWR-D-15-0123.1.
- , 2016b: A numerical study of the 6 May 2012 Tsukuba City supercell tornado. Part II: Mechanisms of tornadogenesis. *Mon. Wea. Rev.*, **144**, 3077–3098, doi:10.1175/MWR-D-15-0122.1.
- , H. Niino, and T. Kato, 2009: Numerical simulation of tornadogenesis in an outer-rainband minisupercell of Typhoon Shanshan on 17 September 2006. *Mon. Wea. Rev.*, **137**, 4238–4260, doi:10.1175/2009MWR2959.1.
- Mason, P. J., and D. J. Thomson, 1992: Stochastic backscatter in large-eddy simulations of boundary layers. *J. Fluid Mech.*, **242**, 51–78, doi:10.1017/S0022112092002271.
- Moeng, C.-H., and J. C. Wyngaard, 1988: Spectral analysis of large-eddy simulations of the convective boundary layer. *J. Atmos. Sci.*, **45**, 3573–3587, doi:10.1175/1520-0469(1988)045<3573:SAOLES>2.0.CO;2.
- Noda, A. T., and H. Niino, 2010: A numerical investigation of a supercell tornado: Genesis and vorticity budget. *J. Meteor. Soc. Japan*, **88**, 135–159, doi:10.2151/jmsj.2010-203.
- Nowotarski, C. J., and P. M. Markowski, 2016: Modifications to the near-storm environment induced by simulated supercell thunderstorms. *Mon. Wea. Rev.*, **144**, 273–293, doi:10.1175/MWR-D-15-0247.1.
- Palmer, R. D., and Coauthors, 2011: Observations of the 10 May 2010 tornado outbreak using OU-PRIME: Potential for new science with high-resolution polarimetric radar. *Bull. Amer. Meteor. Soc.*, **92**, 871–891, doi:10.1175/2011BAMS3125.1.
- Roberts, B., M. Xue, A. D. Schenkman, and D. T. Dawson II, 2016: The role of surface drag in tornadogenesis within an idealized supercell simulation. *J. Atmos. Sci.*, **73**, 3371–3395, doi:10.1175/JAS-D-15-0332.1.
- Rotunno, R., and J. Klemp, 1985: On the rotation and propagation of simulated supercell thunderstorms. *J. Atmos. Sci.*, **42**, 271–292, doi:10.1175/1520-0469(1985)042<0271:OTRAPO>2.0.CO;2.
- Schenkman, A. D., M. Xue, and M. Hu, 2014: Tornadogenesis in a high-resolution simulation of the 8 May 2003 Oklahoma City supercell. *J. Atmos. Sci.*, **71**, 130–154, doi:10.1175/JAS-D-13-073.1.
- , —, and D. T. Dawson II, 2016: The cause of internal outflow surges in a high-resolution simulation of the 8 May 2003 Oklahoma City tornadic supercell. *J. Atmos. Sci.*, **73**, 353–370, doi:10.1175/JAS-D-15-0112.1.
- Skinner, P. S., C. C. Weiss, M. M. French, H. B. Bluestein, P. M. Markowski, and Y. P. Richardson, 2014: VORTEX2 observations of a low-level mesocyclone with multiple internal rear-flank downdraft momentum surges in the 18 May 2010 Dumas, Texas, supercell. *Mon. Wea. Rev.*, **142**, 2935–2960, doi:10.1175/MWR-D-13-00240.1.
- Trapp, R. J., and R. Davies-Jones, 1997: Tornadogenesis with and without a dynamic pipe effect. *J. Atmos. Sci.*, **54**, 113–133, doi:10.1175/1520-0469(1997)054<0113:TAWAD>2.0.CO;2.
- , G. J. Stumpf, and K. L. Manross, 2005: A reassessment of the percentage of tornadic mesocyclones. *Wea. Forecasting*, **20**, 680–687, doi:10.1175/WAF864.1.
- Wicker, L. J., and R. B. Wilhelmson, 1995: Simulation and analysis of tornado development and decay within a three-dimensional supercell thunderstorm. *J. Atmos. Sci.*, **52**, 2675–2703, doi:10.1175/1520-0469(1995)052<2675:SAOTD>2.0.CO;2.
- Xue, M., K. K. Droegemeier, and V. Wong, 2000: The Advanced Regional Prediction System (ARPS)—A multi-scale nonhydrostatic atmospheric simulation and prediction model. Part I: Model dynamics and verification. *Meteor. Atmos. Phys.*, **75**, 161–193, doi:10.1007/s007030070003.
- , and Coauthors, 2001: The Advanced Regional Prediction System (ARPS)—A multi-scale nonhydrostatic atmospheric simulation and prediction tool. Part II: Model physics and applications. *Meteor. Atmos. Phys.*, **76**, 143–165, doi:10.1007/s007030170027.
- , M. Hu, and A. D. Schenkman, 2014: Numerical prediction of the 8 May 2003 Oklahoma City tornadic supercell and embedded tornado using ARPS with the assimilation of WSR-88D data. *Wea. Forecasting*, **29**, 39–62, doi:10.1175/WAF-D-13-00029.1.
- , K. Zhao, M. Wang, Z. Li, and Y. Zheng, 2016: Recent significant tornadoes in China. *Adv. Atmos. Sci.*, **33**, 1209–1217, doi:10.1007/s00376-016-6005-2.